Geostrophically Constrained Flow of Warm Subsurface Waters Into Geometrically Complex Ice Shelf Cavities

Garrett Finucane[1] and Andrew Stewart[2]

[1]University of California, Los Angeles
[2]University of California Los Angeles

April 15, 2024

Abstract

Antarctic ice shelves are losing mass at drastically different rates, primarily due to differing rates of oceanic heat supply to their bases. However, a generalized theory for the inflow of relatively warm water into ice shelf cavities is lacking. This study proposes such a theory based on a geostrophically constrained inflow, combined with a threshold bathymetric elevation, the Highest Unconnected isoBath (HUB), that obstructs warm water access to ice shelf grounding lines. This theory captures ~90% of the variance in melt rates across a suite of idealized process-oriented ocean/ice shelf simulations with quasi-randomized geometries. Applied to observations of ice shelf geometries and offshore hydrography, the theory captures ~80% of the variance in measured ice shelf melt rates. These findings provide a generalized theoretical framework for melt resulting from buoyancy-driven warm water access to geometrically complex Antarctic ice shelf cavities.

Geostrophically Constrained Flow of Warm Subsurface Waters Into Geometrically Complex Ice Shelf Cavities

G. Finucane[1] and A. L. Stewart[1]

[1]Department of Atmospheric and Oceanic Sciences, University of California, Los Angeles, California, USA

Key Points:

- We introduce a new theoretical framework for inflow of warm water into ice shelf cavities based on geostrophically-constrained circulation.
- A new metric, the Highest Unconnected Isobath (HUB), quantifies bathymetric barriers to warm water access in complex geometries.
- Our HUB-informed theoretical framework is able to accurately predict melt rates across a suite of idealized simulations and in observational data.

Corresponding author: Garrett Finucane, `gdf@ucla.edu`

Abstract

Antarctic ice shelves are losing mass at drastically different rates, primarily due to differing rates of oceanic heat supply to their bases. However, a generalized theory for the inflow of relatively warm water into ice shelf cavities is lacking. This study proposes such a theory based on a geostrophically constrained inflow, combined with a threshold bathymetric elevation, the Highest Unconnected isoBath (HUB), that obstructs warm water access to ice shelf grounding lines. This theory captures $\sim 90\%$ of the variance in melt rates across a suite of idealized process-oriented ocean/ice shelf simulations with quasi-randomized geometries. Applied to observations of ice shelf geometries and offshore hydrography, the theory captures $\sim 80\%$ of the variance in measured ice shelf melt rates. These findings provide a generalized theoretical framework for melt resulting from buoyancy-driven warm water access to geometrically complex Antarctic ice shelf cavities.

Plain Language Summary

The floating extensions of Antarctic glaciers ("ice shelves") are losing ice at drastically different rates. A large component of this ice loss is due to melting from below by relatively warm ocean waters, which typically lie hundreds of meters below the surface. Previous studies have attempted to predict ice shelf melt rates using knowledge of the interface between the ice and the ocean. However, these relationships struggle to capture the variations in melt rates around Antarctica, in part because they do not account for obstruction of warm water access by variations in the shape of the seafloor. In this study we introduce a theory for the rate at which warm waters access Antarctica's ice shelves, which indirectly predicts how much the ice shelf melts. This theory is grounded in the assumption that the ocean flow beneath cavities is dominated by the rotation of the earth, and utilizes a novel quantification of seafloor obstruction of warm water inflows. We show that this theory is successful at predicting melt in simulations of ice shelves of different shapes, and in observations of real ice shelves. This work provides a theoretical grounding for melt resulting from warm subsurface waters flowing underneath Antarctic ice shelves.

1 Introduction

The mass loss of Antarctic ice shelves has been accelerating for the past four decades (Paolo et al., 2015; Shepherd et al., 2018). This mass loss has been attributed to the basal melt on the underside of floating ice shelves, which is driven by oceanic heat fluxes (Shepherd et al., 2004; Pritchard et al., 2012). The most vigorous basal melt in Antarctica comes from the intrusion of a subsurface warm water mass, Circumpolar Deep Water (CDW), into ice shelf cavities (Jacobs et al., 1996; Jenkins et al., 2010; Nakayama et al., 2019; Rignot et al., 2019). The depth and temperature of CDW vary around Antarctica (Schmidtko et al., 2014). Ice shelves with shallower (i.e. a thicker intrusion of) CDW and deep troughs tend to have higher melt rates (Nitsche et al., 2017) (see also Fig. S1 in the Supporting Information).

There are various controls on the supply of CDW from the open ocean to the continental shelf. Wind stresses over the continental slope lead to cross-slope Ekman transport that has been linked to variability of CDW heat fluxes across and along the shelf in observations (Assmann et al., 2013; Greene et al., 2017) and models (Spence et al., 2014; Thoma et al., 2008; Dotto et al., 2020; Tamsitt et al., 2021). Wind forcing over the continental shelf can also lead to vigorous deep mixing which erodes the thickness of CDW on the shelf (Caillet et al., 2023; Moorman et al., 2023). Surface buoyancy losses, for example due to sea ice formation in coastal polynyas, are also able to erode the thickness of CDW across the shelf by deepening the mixed layer (Webber et al., 2017; Caillet et al., 2023). In some regions these polynyas produce High Salinity Shelf Water (Nicholls et al., 2009) that fills the ice shelf cavities, blocking the intrusion of CDW (Gwyther et al., 2014; Hellmer et al., 2017; Hazel & Stewart, 2020). In other regions, precipitation onto the ocean in front of the ice shelves can enhance stratification and lead to more lateral transport of CDW to ice shelf faces (Flexas et al., 2022).

Among the various influences on CDW intrusions, previous studies have consistently emphasized the role of bathymetry (Klinck & Dinniman, 2010; Heimbach & Losch, 2012; Nakayama et al., 2019). In particular, deep troughs have been shown to allow CDW to flow mostly unimpeded from offshore into ice shelf cavities in models (Schodlok et al., 2012; St-Laurent et al., 2013; Haigh et al., 2023) and in observations (Assmann et al., 2013; Rintoul et al., 2016). Modeling studies have similarly shown that raising CDW above the height of the main bathymetric obstacles is a necessary condition for pushing cold shelves like the Filchner-Ronne from a low-melt state to a high-melt state (Daae et al., 2020; Hazel & Stewart, 2020).

There have been attempts to link the net melt rate of ice shelves to the bulk properties of the CDW layer and ice shelf cavity geometry (Holland et al., 2008; Little et al., 2009; Lazeroms et al., 2018; Reese et al., 2018; Pelle et al., 2019) but they have all almost exclusively focused on parameterizing the ice ocean boundary layer or plume processes. Burgard et al. (2022) evaluated existing basal melt parameterizations in a regional model that included ice shelves and found that the parameterizations' error was often on the order of the signal. Lazeroms et al. (2018) found that a plume-based melt parameterization could approximately replicate the observed spatial patterns of ice shelf melt, but only with the aid of a tuning parameter that was specific to each ice shelf.

In this study we present a new dynamical framework that determines area-averaged ice shelf melt rates shelf cavities based on a geostrophic constraint on the transport of warm water into the ice shelf cavity (Section 2), rather than based on on processes occurring at the ice-ocean boundary. This allows us to predict the average ice shelf melt rate from the hydrographic conditions outside of an ice shelf cavity. We combine this theory with a novel quantification of the bathymetric obstruction of CDW access, referred to as the Highest Unconnected isoBath (HUB, Section 3). We then test our theory against a suite of idealized model simulations (Section 4) and against observed ice shelf melt rates (Section 5).

2 Theory of geostrophically constrained CDW heat flux into ice shelf cavities

In this section we formulate a theoretical framework for estimating ice shelf cavity melt based on hydrography external to the cavity and its geometry. Previous studies have qualitatively shown that when CDW floods an ice shelf cavity, it fills the cavity horizontally but is deflected downwards to the ice shelf's grounding line by the boundary layer plume that forms at the ice-ocean interface (Nakayama et al., 2019). The change in interface height of CDW inside the ice shelf cavity drives a geostrophic flow parallel to the grounding line until it reaches a wall of the cavity, at which point it is directed towards the grounding line of the ice shelf in a boundary current. This flow regime can be seen in idealized models (e.g. Zhao et al., 2019; De Rydt et al., 2014), as well as in regional models (e.g. Dutrieux et al., 2014; Nakayama et al., 2019). Zhao et al. (2019) showed quantitatively in an idealized model that the transport in this flow regime parallel to the ice shelf grounding line, and subsequently in a boundary current towards the grounding line, could be constrained by the geostrophic velocity driven by the change in depth of the CDW layer inside the cavity. This is analogous to previous scaling theories for buoyancy-driven circulation in enclosed basins in the open ocean (Gnanadesikan, 1999; Nikurashin & Vallis, 2012; Youngs et al., 2020). We will adapt the constraint introduced by Zhao et al. (2019) to estimate the net heat transport associated with the flow of CDW into an ice shelf cavity.

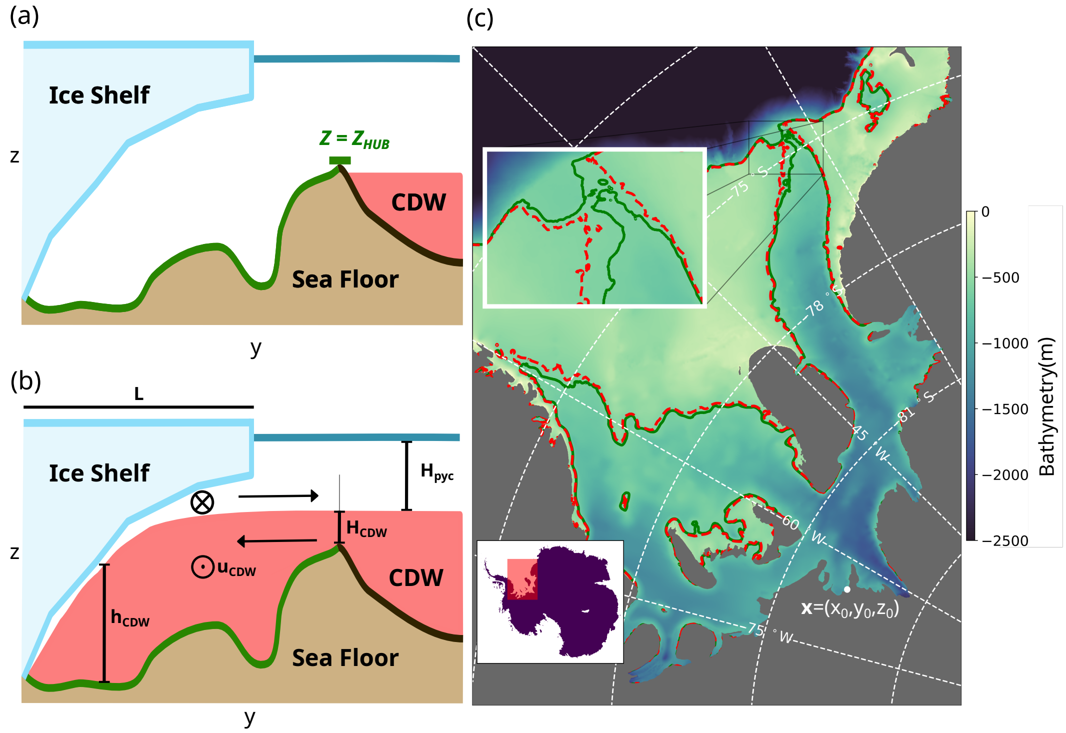

Figure 1. (a) A schematic representation of the highest unconnected isobath (HUB; see Section 3) in two dimensions. All points colored green underneath the ice shelf share the same HUB depth of z_{HUB} (b) An illustration of the proposed watermass structure which is assumed by the theory presented in Section 2. (c) A map of the bathymetry of the Filchner-Ronne ice shelf (FRIS). Regions with grounded ice are filled in gray. The green contour (z=-605 m) surrounds the reference point $\boldsymbol{x}$ but is closed at the shelf break. This means that for water from the open ocean to reach $\boldsymbol{x}$, it must rise shallower than z=-605 m. The red contour (z=-600 m) is open at the shelf break and contains location $\boldsymbol{x}$, meaning that this is the shallowest depth that CDW must reach in order to access $\boldsymbol{x}$. This means the HUB depth for the FRIS is z=-605 m (note that the resolution of our HUB depth calculation is 5m).

To formulate our theory, we idealize the ice shelf cavity circulation as a two-layer flow, comprised of a fresh cold melt layer overlying a warm salty layer (Fig. 1(a & b)). We have labeled the lower layer in our schematic as CDW, although, depending on the specific ice shelf, this could represent other water masses (Thompson et al., 2018). Assuming vertically uniform flow in each layer, the cross-cavity geostrophic transport of CDW may then be formulated as

$$T = \int \mathrm{d}y\, u_{\mathrm{CDW}} h_{\mathrm{CDW}} \sim \int \mathrm{d}y\, \frac{g'_{\mathrm{in}}}{|f|} s_{\mathrm{CDW}} h_{\mathrm{CDW}}, \tag{1}$$

where y is an along-cavity coordinate, h_{CDW} is the thickness of the CDW layer, and u_{CDW} is the cross-cavity CDW velocity. Here we have scaled the cross-cavity flow by the geostrophic shear, i.e. $u_{\mathrm{CDW}} \sim (g'_{\mathrm{in}}/|f|)s_{\mathrm{CDW}}$, where s_{CDW} is the slope of the isopycnal interface between CDW and the overlying waters in the direction from the grounding line to the ice-shelf front, f is the Coriolis parameter, and $g'_{\mathrm{in}} = g(\sigma_{\mathrm{CDW}} - \sigma_{\mathrm{surf}})/\rho_0$ is the reduced gravity determined by the potential density of the CDW layer and surface layer (σ_{CDW} and σ_{surf}, respectively). To further simplify (1), we assume that the interface between the two density layers approximately follows the shape of the ice draft due to melting and mixing processes at the ice-ocean boundary, or equivalently that the gradient of upper layer thickness is much smaller than the gradient of the ice interface, i.e. $s_{\mathrm{CDW}} \approx s_{\mathrm{ice}}$, (see Fig. 1a and Section 4). Note that because we assume the ice shelf is floating in isostatic equilibrium, gradients in ice shelf thickness exert no horizontal pressure gradient force on the fluid. Taking L to be a representative distance from the grounding line to the ice front, we scale (1) as

$$T \sim \frac{g'_{\mathrm{in}}}{|f|} s_{\mathrm{ice}} H_{\mathrm{CDW}} L. \tag{2}$$

Here H_{CDW} is a representative CDW layer thickness, which we assume to be limited by bathymetry between the grounding line and the continental shelf break (see Fig. 1 and Section 3).

To estimate the amount of melt which occurs due to this inflow of CDW, we assume (i) that the net transport of CDW into the cavity is balanced by return flow of freezing-temperature meltwater, and (ii) that the net advective heat transport into the cavity is balanced by heat lost to the ice shelf via basal melting. The latter assumption holds provided that the cavity is in steady state, i.e., over time scales much longer than the cavity flushing time scale (Holland, 2017). Neither assumption takes into account the role of subglacial discharge, which has been shown to be regionally important to basal melt rates (Gwyther et al., 2023; Goldberg et al., 2023). The resulting heat balance can be expressed as

$$\rho_{\mathrm{i}} I_{\mathrm{f}}\, \dot{m} W L \sim \rho_0 C_{\mathrm{p}} T (\theta_{\mathrm{CDW}} - \theta_{\mathrm{surf}}) \tag{3}$$

where W is the cross-cavity width, $\dot{m}$ is the melt rate per unit area, C_{p} is the specific heat capacity of seawater, ρ_0 is a reference ocean density, ρ_{i} is the reference density of ice, I_{f} is the latent heat of melting, θ_{CDW} is the temperature of the CDW, and θ_{surf} is the surface freezing temperature. Substituting (1) into (3) and rearranging leads to the following scaling for the area-averaged melt rate,

$$\dot{m}_{\mathrm{pred}} \equiv \frac{\alpha g'_{\mathrm{in}} \rho_0 C_{\mathrm{p}}}{|f| \rho_{\mathrm{i}} I_{\mathrm{f}} W} s_{\mathrm{ice}} H_{\mathrm{CDW}} (\theta_{\mathrm{CDW}} - \theta_{\mathrm{surf}}). \tag{4}$$

Here we introduce a non-dimensional scaling parameter α, the interpretation of which is discussed further in Section 6.

A shortcoming of this scaling is that in cavities with realistic geometries, the length L and width W are ambiguous. However, in our simulations (in which the ice shelf cavity does have well-defined dimensions; see Section 4) we find that the stratification in the interior of the cavity varies approximately linearly with width, i.e. $g'_{\mathrm{in}}/W \sim g'_{\mathrm{out}}/W_0$, where $W_0 \approx 100\,\mathrm{km}$ is a constant reference width and g'_{out} is the reduced gravity outside the cavity. This relationship yields a predicted area-averaged melt rate that is independent of both the cavity width and length, consistent with the findings of Little et al. (2009),

$$\dot{m}_{\mathrm{pred}} = \frac{\alpha g'_{\mathrm{out}} \rho_0 C_{\mathrm{p}}}{|f| \rho_{\mathrm{i}} I_{\mathrm{f}} W_0} s_{\mathrm{ice}} H_{\mathrm{CDW}} (\theta_{\mathrm{CDW}} - \theta_{\mathrm{surf}}) = \mathcal{C} H_{\mathrm{CDW}} \frac{g'_{\mathrm{out}} s_{\mathrm{ice}}}{|f|} (\theta_{\mathrm{CDW}} - \theta_{\mathrm{surf}}). \tag{5}$$

In the last equality of (5) we have contracted all constant parameters into a single constant of proportionality $\mathcal{C}$. Note that Eq. (5) relates the area-averaged melt rate to quantities derived either from the stratification external to the cavity ($\theta_{\mathrm{CDW}} - \theta_{\mathrm{surf}}$, g'_{out}), the geometry of the cavity (s_{ice}) or a combination of the two (H_{CDW}), and thus serves as our theory for ice shelf melt rates.

3 Quantifying bathymetric obstructions to CDW inflows: the Highest Unconnected isoBath (HUB)

To apply our theory from the previous section in three dimensions we must calculate the thickness of the CDW layer (H_{CDW}), and the temperature of the CDW (θ_{CDW})

at the entrance of the cavity in complex three-dimensional geometries. Because previous studies have shown that the deepest entry points to ice shelf cavities play an important role mediating heat transport (e.g. Walker et al., 2007; St-Laurent et al., 2013), it is crucial that our estimates of CDW thickness and temperature account for these deepest entry points.

To generalize this concept across all Antarctic ice shelves, we formulate a new metric called the Highest Unconnected isoBath (HUB), which may be defined for any reference location on the continental shelf. The HUB may be understood as follows: Consider an ocean that is completely drained of its water, and then slowly fills from its deepest point in such a way that the water is always approximately stationary and in gravitational equilibrium. For any given reference location on the continental shelf, the HUB is defined as the elevation that the water must rise to in order for the reference location to be immersed. More precisely, we can define the HUB for any reference location $\mathbf{x} = (x_0, y_0, z_0)$ on the sea floor of the Antarctic continental shelf. The HUB is equal to the deepest elevation $z_{\text{HUB}} \geq z_0$ such that (x_0, y_0, z_0) can be connected by a three-dimensional path to the open ocean without traversing any depths shallower than z_{HUB} and without traveling through bathymetry. Further discussion of the HUB, including a topological definition, is provided in the Supporting Information.

Fig. 1(a) provides a two-dimensional visualization of the HUB. In this example, all points along the continental shelf highlighted in green share the same HUB, corresponding to the elevation z_{HUB}. CDW must rise to an elevation of at least z_{HUB} in order to reach any of the points highlighted in green. For a real world example, consider the Filchner-Ronne ice shelf; Fig. 1(c) shows the HUB for a reference location $\boldsymbol{x}$ situated at the Filchner-Ronne ice shelf grounding line. This reference location has a HUB of around -605 m (green line). CDW would need rise to an elevation of at least -600 m (red line) in order to reach the reference location from offshore, but would not flood the reference location at a depth of -605 m (green line).

4 Predicting melt in idealized ice shelf cavity simulations

To test our theory of warm water inflows (Section 2), we conduct idealized ocean-ice shelf simulations that span a wide range of cavity geometries and offshore hydrographies (see Fig. 2). Our simulations utilize the MIT general circulation model (Marshall, Adcroft, et al., 1997; Marshall, Hill, et al., 1997) to evolve the state and circulation of the ocean resulting from the the ocean's thermodynamic and mechanical interactions with a static ice shelf (Losch, 2008) (see Supporting Information for more details). To focus on the buoyancy-driven inflow of CDW, we omit other drivers of ocean circulation such as sea ice, tides, and atmospheric forcing. We prescribe an analytical profile of potential temperature and salinity at the northern and eastern boundaries of the model domain (see Fig. 2(a & b) and the Supporting Information), motivated by climatological observations of warm ice shelf cavities (Boyer et al., 2018).

We illustrate the geometry and forcing of our reference case in Fig. 2(a). This ice shelf has dimensions resembling ice shelves in the Amundsen Sea embayment (Morlighem, 2020), being approximately 150km long and 100km wide, with an ice front depth of 250 m and a grounding line depth of 1000 m. The ice shelf slope is linear, and equal to $s_{ice} \approx 0.005$. The HUB of the reference case is approximately 650 m.

We conduct a series of experiments with different ice shelf/bathymetric geometries by varying the continental shelf slope, the ice shelf slope, the cavity width and the extent of the ice shelf front. A full list of the model geometries used in this study is given in the Supporting Information (Table S1 and S5-S8). For all but the reference case we add pseudo-random noise to the sea floor to create more realistic bathymetries with deeper trough-like access pathways. The random noise has a peak wavelength of 62.5km which

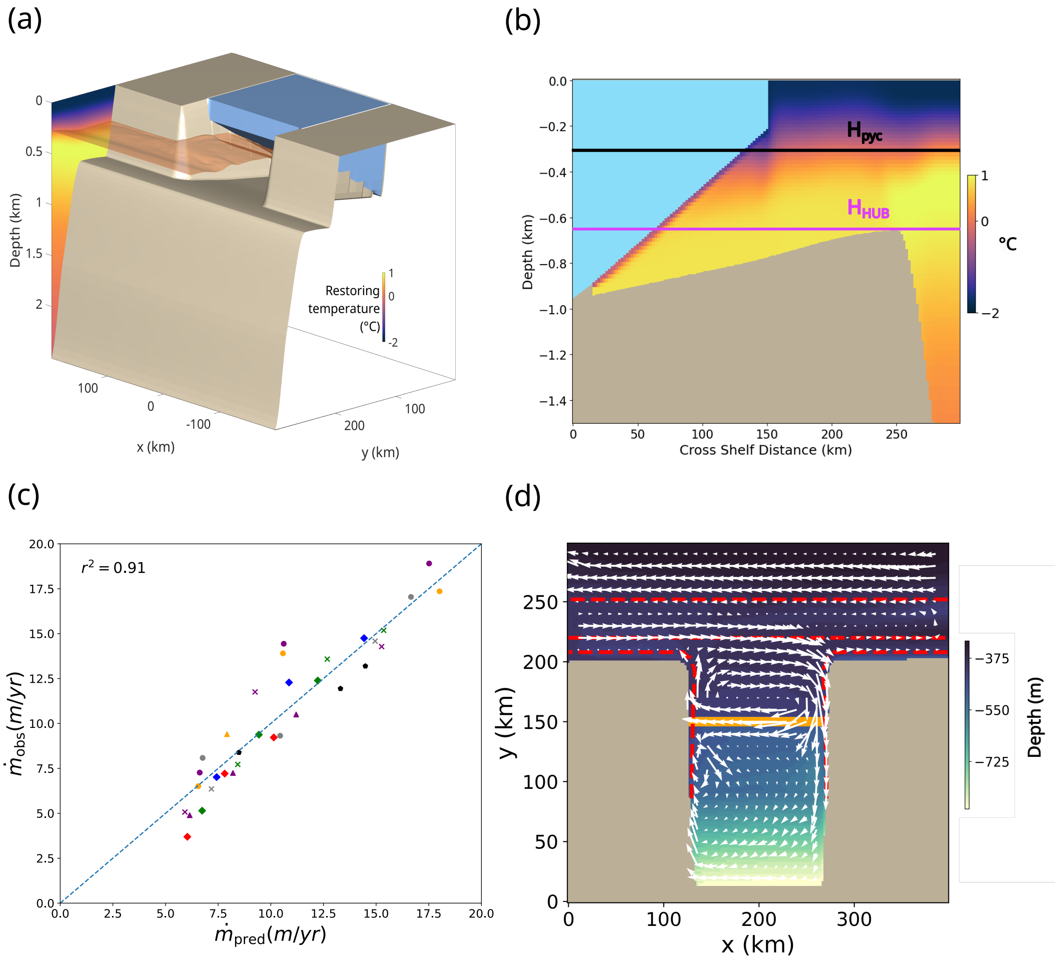

Figure 2. (a) Reference run (ref) model geometry with bathymetry (brown), shelf ice (blue), and boundary temperature forcing colored along the eastern edge of the model domain. (b) Time average cross section of temperature from model run in the same geometry. (c) Linear regression of predicted melts from Eq. 5 against diagnosed area- and time-averaged melt rates across our suite of simulations. Experiments with the same marker and color have the same model geometry, but differing temperature maximum depths: 300 m deeper than, at the same depth as, and 125m shallower than the HUB. The legend provides the simulation names which can be referenced in the Supporting Information (Table S1). (d) Depth of 0.75 °C isotherm is plotted in the background with white arrows denoting the time depth average horizontal velocity below that isotherm. The HUB of the grounding line of this model geometry is shown in red dotted line, and the icefront is shown in the solid orange line.

is roughly the width of troughs in the Amundsen (Walker et al., 2007; Dinniman et al., 2011). The noise is scaled by the water column height (before the noise is applied) in order to prevent the bathymetric variations from closing off portions of the grounding line. For each ice shelf geometry, we conduct three simulations in which we set the depth of the subsurface temperature to 300 m deeper than, at the same depth as, and 125 m shallower than the HUB. In all experiments we use a horizontal grid spacing of 2 km horizontal to adequately resolve mesoscale eddies (St-Laurent et al., 2013; Stewart & Thompson, 2016), although the instantaneous flow fields suggest that the flow is not in a strongly eddying regime. We use a vertical grid consisting of 91 geopotential levels, with resolution varying smoothly from 2 m at the surface to 200 m at the sea floor. The vertical spacing is approximately 20 m at the depth of the ice shelf grounding line. All simulations reach a quasi-steady state by 2.5 years of integration, and are then run for 7.5 additional years for analysis.

We calculate our estimate of area average basal melt rate (Eq. 5) in each simulation using the model's offshore hydrography and cavity geometry. We calculate H_{CDW} by subtracting the HUB from the elevation of the pycnocline depth. The ice slope s_{ice} is determined by the model geometry. We define the CDW temperature θ_{CDW} as the temperature on our prescribed offshore hydrographic profile at the depth of the HUB. Finally, we determine the coefficient $\mathcal{C}$ (and thus α) via linear regression using the diagnosed area-averaged melt rates across our entire suite of simulations. This linear regression yields an α of 0.129. Because this factor is constant across all runs it does not change the correlation with the diagnosed melt rate but rather scales the parameterization output to the correct magnitude.

To evaluate our theory, we compare the predicted ($\dot{m}_{\mathrm{pred}}$) and diagnosed ($\dot{m}_{\mathrm{model}}$) area-averaged ice shelf melt rates in Fig. 2(c). We find that the predicted melt rates explain 91% of the variance in the diagnosed melt rates across all simulations. Experiments with the same geometry (which have the same marker shape/color in Fig. 2(c)) show increasing predicted and diagnosed melt rates in simulations with higher offshore CDW. The ability of our parameterization to predict the diagnosed melt rate suggests that the geometric aspects of the cavity that are of first order importance are the large scale ice shelf slope and the deepest depth of CDW access (the HUB). These results indicate that our theory is successfully capturing the leading order dynamics of warm water inflows in this idealized model.

5 Predicting observed ice shelf melt rates

The parameterization from Section 2 is able to accurately predict melt in a geometrically simple model designed to isolate the dynamics of warm water inflows (Section 4). We now test our prediction of basal melt using observations around Antarctica. We draw on observations of near-Antarctic hydrography, as synthesized in the World Ocean Atlas 2018 (Boyer et al., 2018) annual climatology, and on satellite-derived estimates of ice shelf melt from Adusumilli et al. (2020).

The theory encapsulated by Eq. (5) assumes a simplified geometry that contrasts with the complex geometries of natural ice shelf cavities; for example, the depth of real ice shelf grounding lines vary spatially, as does the slope of the ice. In order to generalize the theory to real ice shelf cavity geometries, we compute bulk estimates of the different parameters in our theory (Eq. (5)). Specifically, for a given ice shelf we identify all points from the Bedmachine (Morlighem, 2020) 500 m resolution grid which contain grounded ice and are adjacent to floating ice as grounding line points, and then estimate the hydrographic parameters H_{CDW}, g'_{out} and $\theta_{\mathrm{CDW}} - \theta_{\mathrm{surf}}$ for each grounding line point. We then group those grounding line points by ice shelf and average each parameter separately to formulate our prediction of the area-averaged melt rate,

$$\dot{m}_{\mathrm{pred}} \equiv \mathcal{C}\langle H_{\mathrm{CDW}}\rangle \overline{s_{\mathrm{ice}}} \langle g'_{\mathrm{out}}\rangle \langle f^{-1}\rangle \langle \theta_{\mathrm{CDW}} - \theta_{\mathrm{surf}}\rangle, \tag{6}$$

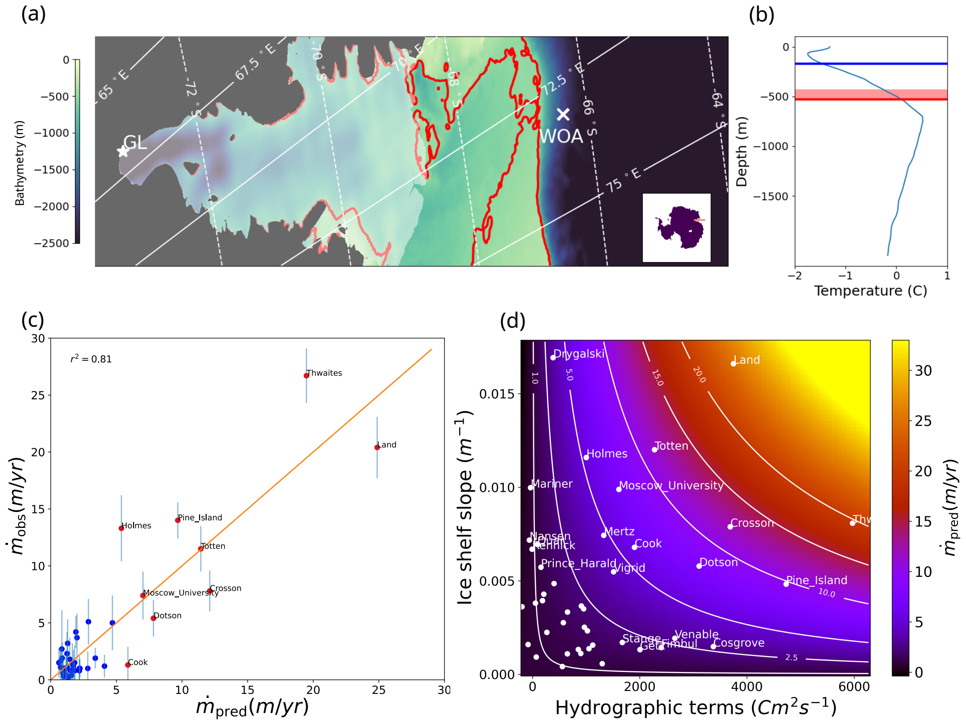

Figure 3. Application of our theory to predict circum-Antarctic ice shelf melt rates. (a) An illustration of the off-shore hydrographic cast selection methodology for a single point on the Amery ice shelf grounding line. The bathymetry of the Amery Ice shelf is colored in blue and green, floating shelf ice in translucent white and grounded ice in gray. The red line depicts the HUB depth for the starred grounding line point (GL). The WOA hydrographic cast that is used to estimate heat transport toward point "GL" is labeled "WOA", and is selected as decribed in Section 5. (b) The hydrography at the point labeled "WOA" in panel (a), with the HUB for point "GL" marked by a red line, and the calculated pycnocline marked by a blue line. (c) The linear regression of predicted melt rate from Eq. 5 against observed melt rates from Adusumilli et al. (2020). Error bars are estimates of observational error from Adusumilli et al. (2020). (d) Predicted melt rate (colors and white contours) as a function of different parameters in our theory (Eq. 6). On the x-axis the grounding line-averaged hydrographic terms, $\langle H_{\text{CDW}}\rangle\langle g'_{\text{out}}\rangle\langle\theta_{\text{CDW}} - \theta_{\text{surf}}\rangle\langle|f^{-1}|\rangle$, and on the y-axis the cavity-averaged ice shelf slope $\overline{s_{\text{ice}}}$. Antarctic ice shelves' locations in this parameter space are indicated by white circles.

where $\langle\cdot\rangle$ denotes an average over all grounding line points within the ice shelf and $\bar{\cdot}$ denotes an average over the whole ice shelf area. We treat the ice shelf slope s_{ice} differently because this parameter is related to the geometry of the whole cavity, rather than external hydrographic properties. The Supporting Information specifies how we choose an appropriate offshore hydrographic cast at the 1500m isobath for each grounding line point using the HUB, and how we calculate the temperature of the CDW layer (θ_{CDW}), the thickness of the CDW layer (H_{CDW}), the exterior reduced gravity (g'_{CDW}), and the bulk ice shelf slope s_{ice}.

In Fig. 3(c) we compare the melt predicted by our theory (6) against the satellite-derived estimates of basal melt and accompanying uncertainty from Adusumilli et al. (2020). We determine the constant prefactor $\mathcal{C}$ via linear regression, which yields $\alpha = 0.105$ (see Eq. 5). We find that our theoretical prediction explains $\sim$ 81% of the variance in the observed melt rates. This can be contrasted with Fig. S4 and Fig. S5 which show the correlation between melt and just the thermal forcing term and just the slope term of our parameterization. This suggests that, for ice shelves in which the melt rates are driven by CDW inflows, variations in these melt rates are accurately accounted for by our geostrophic constraint on the inflow of CDW into the cavity. As expected, the theory does poorly at predicting the melt rate in “cold” cavities in which CDW inflows do not dominate the melt rate. Note that in “cold” ice shelf cavities, the error bars on observations are often nearly the same magnitude as the signal.

In Fig. 3(d) we use our theory to determine the relative importance of ice draft slope versus external hydrography in the predicted ice shelf melt rates. Specifically, we map the melt rates in a parameter space defined by two parts of Eq. (6): the cavity-averaged ice shelf slope, $\overline{s_{\mathrm{ice}}}$, and the rest of the equation, $\langle H_{\mathrm{CDW}}\rangle\langle g'_{\mathrm{out}}\rangle\langle\theta_{\mathrm{CDW}} - \theta_{\mathrm{surf}}\rangle\langle|f^{-1}|\rangle$. This decomposition shows that ice shelves with similarly high rates of melt may have an abundance of warm CDW that has access to the cavity, *e.g.* Dotson ice shelf, or from a relatively steep ice draft, *e.g.* Drygalski ice shelf. Furthermore, neglecting changes in ice shelf slope, the theory predicts that ice shelves with gentle slopes (e.g. the eastern Ross) would exhibit little change in melt rate even if CDW was to rise significantly, in contrast to steeply sloping ice shelves like the Totten.

6 Discussion and Conclusion

This study presents a novel constraint on the net heat transport into ice shelf cavities, and thus, indirectly, on the area-averaged melt rates of the ice shelves. The guiding principle of our theory (Section 2) is that if CDW is shallower than the dominant bathymetric obstacle blocking the cavity, its flow into the cavity is geostrophically constrained by the along-cavity density gradient established by the interface between CDW and meltwater within the cavity. Applying scaling arguments, we obtain a relationship Eq. (5) between the area-averaged melt, the slope of the ice shelf draft, and the thickness, temperature and density anomaly of CDW. Motivated by previous findings that the deepest troughs in the continental shelf play a key role in funneling CDW toward ice shelves, (e.g. Walker et al., 2007; St-Laurent et al., 2013) we further introduce a new metric called the Highest Unconnected isoBath that identifies the key depth which offshore waters must reach to flood ice shelf cavities (Section 3). We use the HUB to determine the waters that can access a given ice shelf cavity, which in turn constrains the along-cavity density gradient and thus the net heat transport in our theory. We evaluate our theoretical prediction across a suite of idealized model simulations (Section 4), and find that it explains 90% of the variance of the diagnosed melt rates. Finally, we apply the theory to predict observational estimates of ice shelf melt rates (Adusumilli et al., 2020), and find that the theory explains 80% of the variance in melt rate across all Antarctic ice shelves (Section 5). Taken together, these findings indicate that our geostrophic constraint captures the leading-order dynamics of the net heat transport into warm Antarctic ice shelf cavities.

Our formulation contrasts from existing parameterizations of ice shelf melt by focusing on the transport of heat into the cavity using solely the offshore hydrographic properties and the morphology of the ice shelf rather than the dynamics of melt once warm water reaches the ice shelf face. This means that our theory predicts only one area averaged basal melt rate for an ice shelf cavity, and does not produce spatially varying maps of ice shelf melt.

In deriving and applying our theoretical estimate of the heat flux into ice shelf cavities Eq. (5) we have made a number of simplifying assumptions, discussed in Section 2. One is that we neglect the effects of wind and surface buoyancy forcing, whereas previous observational and modeling studies indicate that these effects may play a key role in controlling ice shelf melt rates (Webber et al., 2017; Thoma et al., 2008; Hattermann, 2018; Guo et al., 2022; Silvano et al., 2022). We also assume that the cavity circulation is in equilibrium with the external oceanic conditions, *i.e.* that the net heat transport into the cavity is completely used for ice shelf melt. We might expect this assumption to fail on time scales shorter than the flushing time scale of the cavity (Holland, 2017), on which transient heat storage in the cavity and ice shelf boundary layer/plume dynamics more directly dictate the melt rate (Lazeroms et al., 2018). Our theory also predicts that the melt rate is entirely determined by the ice shelf geometry and the external hydrography, in contrast with previous studies showing that circulation within ice shelves can exhibit bi-stable states (Hellmer et al., 2017; Moorman et al., 2023; Caillet et al., 2023). Future work is required to reconcile our theory with previous theories for bi-stability of ice shelf cavity circulation and melt rates (Hazel & Stewart, 2020). Our model configuration (Section 4) is reflective only of warm ice shelves by virtue of the prescribed offshore hydrography and lack of dense water formation. Future work is needed to understand if cold shelves are similarly geostrophically constrained.

An outstanding question from this study is the extent to which other processes influencing the ice shelf-ocean boundary layer (or parameterizations thereof) are compatible with our geostrophic theory. For example, tides have been shown to increase melt rates across Antarctica (Richter et al., 2022), simulated basal melt has been shown to be dependent on vertical resolution (Schodlok et al., 2016), and melt has been shown to be sensitive to the parameterization of turbulent transfer into the ice-ocean boundary layer (Jourdain et al., 2017). Such processes could conceivably change elements of the physics encapsulated by the scaling prefactor α, *i.e.* the partitioning of the geostrophic shear between the CDW and melt water layers, the cavity width-dependent relationship between external and internal reduced gravity, and/or the change in CDW thickness between the shelf break and the ice shelf front. In this case we might expect that including a dependence of α on the tides, vertical resolution, and turbulent transfer parameterization to yield more accurate predictions of melt rate. However, it is not yet clear whether incorporating such dependencies into α is necessary: an alternative hypothesis is that changes in the processes occurring in the modeled/observed ice-ocean boundary layer lead to feedbacks on the stratification outside the cavity, such that the melt rate remains consistent with our geostrophic constraint. This hypothesis is supported by the close agreement between the values of α inferred from our idealized model simulations ($\alpha = 1.29$) versus observations ($\alpha = .105$). However, this agreement could be coincidence, so we propose further experiments in a regional ocean/sea ice/ice shelf model configuration to explore the robustness of α more thoroughly.

To our knowledge, this is the first time satellite-derived melt has been successfully estimated using offshore hydrographic observations without a tuning for every ice shelf. The framework succeeds despite observational error in the bathymetric, hydrographic, and basal melt measurements. We argue this could lead to improved parameterizations with better predictive capabilities. The theory we introduce also provides insight into the relative importance of geometry and hydrographic forcing in ice shelves around Antarctica.

7 Open Research

The observational hydrographic data used in this project is available on the National Centers for Environmental Information website (`https://www.ncei.noaa.gov/access/metadata/landing-page/bin/iso?id=gov.noaa.nodc:NCEI-WOA18`). BedMachine version 2 bathymetric and ice shelf thickness data is available from the National Snow and Ice Data Center (`https://nsidc.org/data/nsidc-0756/versions/2`). Antarctic boundaries from satellite radar are available from the NSIDC as well (`https://nsidc.org/data/nsidc-0709/versions/2`). Satellite derived estimates of basal melt from Adusumilli et al. (2020) can be found in the supplementary information (`https://doi.org/10.1038/s41561-020-0616-z`). The analysis code for the observational work detailed in this paper is freely available on GitHub (`https://doi.org/10.5281/zenodo.10891688`). The modeling setup and analysis code for the modeling work in this paper is also available on GitHub (`https://doi.org/10.5281/zenodo.10892819`).

Acknowledgments

This material is based in part upon work supported by the National Science Foundation under Grant Numbers OCE-1751386 and OPP-2220968, and by the National Aeronautics and Space Administration ROSES Physical Oceanography program under grant number 80NSSC23K0357. This work used the Extreme Science and Engineering Discovery Environment (XSEDE, Towns et al. (2014)), which is supported by National Science Foundation grant number ACI-1548562. Without implying their endorsement, the authors thank Clara Burgard and Ken Zhao for various discussions that improved this study.

References

Adusumilli, S., Fricker, H. A., Medley, B., Padman, L., & Siegfried, M. R. (2020). Interannual variations in meltwater input to the Southern Ocean from Antarctic ice shelves. *Nature Geoscience*, *13*(9), 616–620. doi: 10.1038/s41561-020-0616-z

Assmann, K. M., Jenkins, A., Shoosmith, D. R., Walker, D. P., Jacobs, S. S., & Nicholls, K. W. (2013). Variability of Circumpolar Deep Water transport onto the Amundsen Sea Continental shelf through a shelf break trough. *Journal of Geophysical Research: Oceans*, *118*(12), 6603–6620. doi: 10.1002/2013JC008871

Boyer, T. P., Garcia, H. E., Locarnini, R. A., Zweng, M. M., Mishonov, A. V., Reagan, J. R., ... Smolyar, I. V. (2018). *World ocean atlas 2018.* NOAA National Centers for Environmental Information.

Burgard, C., Jourdain, N. C., Reese, R., Jenkins, A., & Mathiot, P. (2022). An assessment of basal melt parameterisations for Antarctic ice shelves. *The Cryosphere Discussions*, 1–56. doi: 10.5194/tc-2022-32

Caillet, J., Jourdain, N. C., Mathiot, P., Hellmer, H. H., & Mouginot, J. (2023). Drivers and Reversibility of Abrupt Ocean State Transitions in the Amundsen Sea, Antarctica. *Journal of Geophysical Research: Oceans*, *128*(1), e2022JC018929. doi: 10.1029/2022JC018929

Daae, K., Hattermann, T., Darelius, E., Mueller, R. D., Naughten, K. A., Timmermann, R., & Hellmer, H. H. (2020). Necessary Conditions for Warm Inflow Toward the Filchner Ice Shelf, Weddell Sea. *Geophysical Research Letters*, *47*(22). doi: 10.1029/2020GL089237

De Rydt, J., Holland, P. R., Dutrieux, P., & Jenkins, A. (2014). Geometric and oceanographic controls on melting beneath Pine Island Glacier. *Journal of Geophysical Research: Oceans*, *119*(4), 2420–2438. doi: 10.1002/2013JC009513

Dinniman, M. S., Klinck, J. M., & Smith, W. O. (2011). A model study of Circumpolar Deep Water on the West Antarctic Peninsula and Ross Sea continental shelves. *Deep Sea Research Part II: Topical Studies in Oceanography*, *58*(13), 1508–1523. doi: 10.1016/j.dsr2.2010.11.013

Dotto, T. S., Naveira Garabato, A. C., Wåhlin, A. K., Bacon, S., Holland, P. R., Kimura, S., ... Jenkins, A. (2020). Control of the Oceanic Heat Content of the Getz-Dotson Trough, Antarctica, by the Amundsen Sea Low. *Journal of Geophysical Research: Oceans*, *125*(8), e2020JC016113. doi: 10.1029/2020JC016113

Dutrieux, P., De Rydt, J., Jenkins, A., Holland, P. R., Ha, H. K., Lee, S. H., ... Schröder, M. (2014). Strong Sensitivity of Pine Island Ice-Shelf Melting to Climatic Variability. *Science*, *343*(6167). doi: 10.1126/science.1244341

Flexas, M. M., Thompson, A. F., Schodlok, M. P., Zhang, H., & Speer, K. (2022). Antarctic Peninsula warming triggers enhanced basal melt rates throughout West Antarctica. *Science Advances*, *8*(32), eabj9134. doi: 10.1126/sciadv.abj9134

Gnanadesikan, A. (1999). A simple predictive model for the structure of the oceanic pycnocline. *Science (New York, N.Y.)*, *283*(5410), 2077–2079. doi: 10.1126/science.283.5410.2077

Goldberg, D. N., Twelves, A. G., Holland, P. R., & Wearing, M. G. (2023). The Non-Local Impacts of Antarctic Subglacial Runoff. *Journal of Geophysical Research: Oceans*, *128*. Retrieved from `https://onlinelibrary.wiley.com/doi/abs/10.1029/2023JC019823` doi: 10.1029/2023JC019823

Greene, C. A., Blankenship, D. D., Gwyther, D. E., Silvano, A., & van Wijk, E. (2017). Wind causes Totten Ice Shelf melt and acceleration. *Science Advances*, *3*(11), e1701681. doi: 10.1126/sciadv.1701681

Guo, Y., Bachman, S., Bryan, F., & Bishop, S. (2022). Increasing Trends in Oceanic Surface Poleward Eddy Heat Flux Observed Over the Past Three Decades. *Geophysical Research Letters*, *49*(16), e2022GL099362. doi: 10.1029/2022GL099362

Gwyther, D. E., Dow, C. F., Jendersie, S., Gourmelen, N., & Galton-Fenzi, B. K. (2023). Subglacial Freshwater Drainage Increases Simulated Basal Melt of the Totten Ice Shelf. *Geophysical Research Letters*, *50*(12), e2023GL103765. doi: 10.1029/2023GL103765

Gwyther, D. E., Galton-Fenzi, B. K., Hunter, J. R., & Roberts, J. L. (2014). Simulated melt rates for the Totten and Dalton ice shelves. *Ocean Science*, *10*(3), 267–279. doi: 10.5194/os-10-267-2014

Haigh, M., Holland, P. R., & Jenkins, A. (2023). The Influence of Bathymetry Over Heat Transport Onto the Amundsen Sea Continental Shelf. *Journal of Geophysical Research: Oceans*, *128*(5), e2022JC019460. doi: 10.1029/2022JC019460

Hattermann, T. (2018). Antarctic Thermocline Dynamics along a Narrow Shelf with Easterly Winds. *Journal of Physical Oceanography*, *48*(10), 2419–2443. doi: 10.1175/JPO-D-18-0064.1

Hazel, J. E., & Stewart, A. L. (2020). Bistability of the Filchner-Ronne Ice Shelf Cavity Circulation and Basal Melt. *Journal of Geophysical Research: Oceans*, *125*(4), e2019JC015848. doi: https://doi.org/10.1029/2019JC015848

Heimbach, P., & Losch, M. (2012). Adjoint sensitivities of sub-ice-shelf melt rates to ocean circulation under the Pine Island Ice Shelf, West Antarctica. *Annals of Glaciology*, *53*(60), 59–69. doi: 10.3189/2012/AoG60A025

Hellmer, H. H., Kauker, F., Timmermann, R., & Hattermann, T. (2017). The Fate of the Southern Weddell Sea Continental Shelf in a Warming Climate. *Journal of Climate*, *30*(12), 4337–4350. doi: 10.1175/JCLI-D-16-0420.1

Holland, P. R. (2017). The Transient Response of Ice Shelf Melting to Ocean Change. *Journal of Physical Oceanography*, *47*(8), 2101–2114. doi: 10.1175/JPO-D-17-0071.1

Holland, P. R., Jenkins, A., & Holland, D. M. (2008). The Response of Ice Shelf

Basal Melting to Variations in Ocean Temperature. *Journal of Climate*, *21*(11), 2558–2572. doi: 10.1175/2007JCLI1909.1

Jacobs, S. S., Hellmer, H. H., & Jenkins, A. (1996). Antarctic Ice Sheet melting in the southeast Pacific. *Geophysical Research Letters*, *23*(9), 957–960. doi: 10.1029/96GL00723

Jenkins, A., Dutrieux, P., Jacobs, S. S., McPhail, S. D., Perrett, J. R., Webb, A. T., & White, D. (2010). Observations beneath Pine Island Glacier in West Antarctica and implications for its retreat. *Nature Geoscience*, *3*(7), 468–472. doi: 10.1038/ngeo890

Jourdain, N. C., Mathiot, P., Merino, N., Durand, G., Le Sommer, J., Spence, P., … Madec, G. (2017). Ocean circulation and sea-ice thinning induced by melting ice shelves in the Amundsen Sea. *Journal of Geophysical Research: Oceans*, *122*(3). Retrieved 2024-03-29, from `https://onlinelibrary.wiley.com/doi/abs/10.1002/2016JC012509` doi: 10.1002/2016JC012509

Klinck, J. M., & Dinniman, M. S. (2010). Exchange across the shelf break at high southern latitudes. *Ocean Science*, *6*(2), 513–524. doi: 10.5194/os-6-513-2010

Lazeroms, W. M. J., Jenkins, A., Gudmundsson, G. H., & van de Wal, R. S. W. (2018). Modelling present-day basal melt rates for Antarctic ice shelves using a parametrization of buoyant meltwater plumes. *The Cryosphere*, *12*(1), 49–70. doi: 10.5194/tc-12-49-2018

Little, C. M., Gnanadesikan, A., & Oppenheimer, M. (2009). How ice shelf morphology controls basal melting. *Journal of Geophysical Research: Oceans*, *114*(C12). doi: 10.1029/2008JC005197

Losch, M. (2008). Modeling ice shelf cavities in a z coordinate ocean general circulation model. *Journal of Geophysical Research: Oceans*, *113*(C8). doi: 10.1029/2007JC004368

Marshall, J., Adcroft, A., Hill, C., Perelman, L., & Heisey, C. (1997). A finite-volume, incompressible Navier Stokes model for studies of the ocean on parallel computers. *Journal of Geophysical Research: Oceans*, *102*(C3), 5753–5766. doi: 10.1029/96JC02775

Marshall, J., Hill, C., Perelman, L., & Adcroft, A. (1997). Hydrostatic, quasi-hydrostatic, and nonhydrostatic ocean modeling. *Journal of Geophysical Research: Oceans*, *102*(C3), 5733–5752. doi: 10.1029/96JC02776

Moorman, R., Thompson, A. F., & Wilson, E. A. (2023). Coastal Polynyas Enable Transitions Between High and Low West Antarctic Ice Shelf Melt Rates. *Geophysical Research Letters*, *50*(16), e2023GL104724. doi: 10.1029/2023GL104724

Morlighem, M. (2020). *Measures bedmachine antarctica, version 2.* NASA National Snow and Ice Data Center Distributed Active Archive Center.

Nakayama, Y., Manucharyan, G., Zhang, H., Dutrieux, P., Torres, H. S., Klein, P., … Menemenlis, D. (2019). Pathways of ocean heat towards Pine Island and Thwaites grounding lines. *Scientific Reports*, *9*(1), 16649. doi: 10.1038/s41598-019-53190-6

Nicholls, K. W., Østerhus, S., Makinson, K., Gammelsrød, T., & Fahrbach, E. (2009). Ice-ocean processes over the continental shelf of the southern Weddell Sea, Antarctica: A review. *Reviews of Geophysics*, *47*(3). doi: 10.1029/2007RG000250

Nikurashin, M., & Vallis, G. (2012). A Theory of the Interhemispheric Meridional Overturning Circulation and Associated Stratification. *Journal of Physical Oceanography*, *42*(10), 1652–1667. doi: 10.1175/JPO-D-11-0189.1

Nitsche, F. O., Porter, D., Williams, G., Cougnon, E. A., Fraser, A. D., Correia, R., & Guerrero, R. (2017). Bathymetric control of warm ocean water access along the East Antarctic Margin. *Geophysical Research Letters*, *44*(17), 8936–8944. doi: 10.1002/2017GL074433

Paolo, F. S., Fricker, H. A., & Padman, L. (2015). Volume loss from Antarctic ice

shelves is accelerating. *Science*, *348*(6232), 327–331. doi: 10.1126/science.aaa0940
Pelle, T., Morlighem, M., & Bondzio, J. H. (2019). Brief communication: PICOP, a new ocean melt parameterization under ice shelves combining PICO and a plume model. *The Cryosphere*, *13*(3), 1043–1049. doi: 10.5194/tc-13-1043-2019
Pritchard, H. D., Ligtenberg, S. R. M., Fricker, H. A., Vaughan, D. G., van den Broeke, M. R., & Padman, L. (2012). Antarctic ice-sheet loss driven by basal melting of ice shelves. *Nature*, *484*(7395), 502–505. doi: 10.1038/nature10968
Reese, R., Albrecht, T., Mengel, M., Asay-Davis, X., & Winkelmann, R. (2018). Antarctic sub-shelf melt rates via PICO. *The Cryosphere*, *12*(6). Retrieved from `https://tc.copernicus.org/articles/12/1969/2018/` doi: 10.5194/tc-12-1969-2018
Richter, O., Gwyther, D. E., King, M. A., & Galton-Fenzi, B. K. (2022). The impact of tides on Antarctic ice shelf melting. *The Cryosphere*(4). Retrieved 2024-03-27, from `https://tc.copernicus.org/articles/16/1409/2022/` doi: 10.5194/tc-16-1409-2022
Rignot, E., Mouginot, J., Scheuchl, B., van den Broeke, M., van Wessem, M. J., & Morlighem, M. (2019). Four decades of Antarctic Ice Sheet mass balance from 1979–2017. *Proceedings of the National Academy of Sciences*, *116*(4), 1095–1103. doi: 10.1073/pnas.1812883116
Rintoul, S. R., Silvano, A., Pena-Molino, B., van Wijk, E., Rosenberg, M., Greenbaum, J. S., & Blankenship, D. D. (2016). Ocean heat drives rapid basal melt of the Totten Ice Shelf. *Science Advances*, *2*(12), e1601610. doi: 10.1126/sciadv.1601610
Schmidtko, S., Heywood, K. J., Thompson, A. F., & Aoki, S. (2014). Multidecadal warming of Antarctic waters. *Science*, *346*(6214), 1227–1231. doi: 10.1126/science.1256117
Schodlok, M. P., Menemenlis, D., Rignot, E., & Studinger, M. (2012). Sensitivity of the ice-shelf/ocean system to the sub-ice-shelf cavity shape measured by NASA IceBridge in Pine Island Glacier, West Antarctica. *Annals of Glaciology*, *53*(60). doi: 10.3189/2012AoG60A073
Schodlok, M. P., Menemenlis, D., & Rignot, E. J. (2016). Ice shelf basal melt rates around Antarctica from simulations and observations. *Journal of Geophysical Research: Oceans*, *121*(2). Retrieved from `https://onlinelibrary.wiley.com/doi/abs/10.1002/2015JC011117` doi: 10.1002/2015JC011117
Shepherd, A., Fricker, H. A., & Farrell, S. L. (2018). Trends and connections across the Antarctic cryosphere. *Nature*, *558*(7709), 223–232. doi: 10.1038/s41586-018-0171-6
Shepherd, A., Wingham, D., & Rignot, E. (2004). Warm ocean is eroding West Antarctic Ice Sheet. *Geophysical Research Letters*, *31*(23). doi: 10.1029/2004GL021106
Silvano, A., Holland, P. R., Naughten, K. A., Dragomir, O., Dutrieux, P., Jenkins, A., … Naveira Garabato, A. C. (2022). Baroclinic Ocean Response to Climate Forcing Regulates Decadal Variability of Ice-Shelf Melting in the Amundsen Sea. *Geophysical Research Letters*, *49*(24), e2022GL100646. doi: 10.1029/2022GL100646
Spence, P., Griffies, S. M., England, M. H., Hogg, A. M., Saenko, O. A., & Jourdain, N. C. (2014). Rapid subsurface warming and circulation changes of Antarctic coastal waters by poleward shifting winds. *Geophysical Research Letters*, *41*(13), 4601–4610. doi: 10.1002/2014GL060613
Stewart, A. L., & Thompson, A. F. (2016). Eddy Generation and Jet Formation via Dense Water Outflows across the Antarctic Continental Slope. *Journal of Physical Oceanography*, *46*(12), 3729–3750. doi: 10.1175/JPO-D-16-0145.1
St-Laurent, P., Klinck, J. M., & Dinniman, M. S. (2013). On the Role of

Coastal Troughs in the Circulation of Warm Circumpolar Deep Water on Antarctic Shelves. *Journal of Physical Oceanography*, *43*(1), 51–64. doi: 10.1175/JPO-D-11-0237.1

Tamsitt, V., England, M. H., Rintoul, S. R., & Morrison, A. K. (2021). Residence Time and Transformation of Warm Circumpolar Deep Water on the Antarctic Continental Shelf. *Geophysical Research Letters*, *48*(20), e2021GL096092. doi: 10.1029/2021GL096092

Thoma, M., Jenkins, A., Holland, D., & Jacobs, S. (2008). Modelling Circumpolar Deep Water intrusions on the Amundsen Sea continental shelf, Antarctica. *Geophysical Research Letters*, *35*(18). doi: 10.1029/2008GL034939

Thompson, A. F., Stewart, A. L., Spence, P., & Heywood, K. J. (2018). The Antarctic Slope Current in a Changing Climate. *Reviews of Geophysics*, *56*(4), 741–770. doi: https://doi.org/10.1029/2018RG000624

Towns, J., Cockerill, T., Dahan, M., Foster, I., Gaither, K., Grimshaw, A., ... Wilkins-Diehr, N. (2014, Sept). XSEDE: Accelerating scientific discovery. *Computing in Science Engineering*, *16*(5), 62-74. doi: 10.1109/MCSE.2014.80

Walker, D. P., Brandon, M. A., Jenkins, A., Allen, J. T., Dowdeswell, J. A., & Evans, J. (2007). Oceanic heat transport onto the Amundsen Sea shelf through a submarine glacial trough. *Geophysical Research Letters*, *34*(2). doi: 10.1029/2006GL028154

Webber, B. G. M., Heywood, K. J., Stevens, D. P., Dutrieux, P., Abrahamsen, E. P., Jenkins, A., ... Kim, T. W. (2017). Mechanisms driving variability in the ocean forcing of Pine Island Glacier. *Nature Communications*, *8*(1), 14507. doi: 10.1038/ncomms14507

Youngs, M. K., Ferrari, R., & Flierl, G. R. (2020). Basin-Width Dependence of Northern Deep Convection. *Geophysical Research Letters*, *47*(15), e2020GL089135. doi: 10.1029/2020GL089135

Zhao, K. X., Stewart, A. L., & McWilliams, J. C. (2019). Sill-Influenced Exchange Flows in Ice Shelf Cavities. *Journal of Physical Oceanography*, *49*(1), 163–191. doi: 10.1175/JPO-D-18-0076.1

Geostrophically Constrained Flow of Warm Subsurface Waters Into Geometrically Complex Ice Shelf Cavities

G. Finucane [1]and A. L. Stewart [1]

[1]Department of Atmospheric and Oceanic Sciences, University of California, Los Angeles, California, USA

Contents of this file

Text S1. Topological definition of HUB.

The main text provides a qualitative definition and visual illustration of the Highest Unconnected isoBath (HUB), which we use to identify the bathymetric constraints on warm water inflows into ice shelf cavities. Here we provide a more rigorous topological defintion for clarity.

Given a continuous function of elevation $Z(x, y) : \mathrm{C} \subset \mathbb{R}^2 \rightarrow \mathrm{D} \subset \mathbb{R}$ And given a subset of points $\mathrm{O} \subset \mathbb{C}$ which are designated open ocean points. The HUB for any point

$x \in$ C is the greatest z_{HUB} such that x is not path connected to any points in O in the set $Z^{-1}((-\infty, z_{\mathrm{HUB}}))$.

A topological space (X, τ) *is said to be path-connected (or pathwise connected) if for each pair of (distinct) points a and b of X there exists a continuous mapping* $f : [0,1] \to (X, \tau)$*, such that* $f(0) = a$ *and* $f(1) = b$*. The mapping f is said to be a path joining a to b.* (Definition from "Topology Without Tears" Morris 2020).

Text S2. Additional information on the model configuration

The text in this section provides additional information on the model configuration in the interest of reproducibility. The text below summarizes salient model configuration and parameter choices, but is not exhaustive. For any details of the model configuration that are not covered here, the reader is referred to the model configuration code, a link to which is provided in the main text.

The MITgcm model we use solves the hydrostatic Boussinesq equations to evolve the state of the ocean . It uses the non-linear equation of state of McDougall, Jackett, Wright, and Feistel (2003), which is abbreviated as "MDJWF" in the MITgcm model code.

Along the northern and eastern boundaries we prescribe the temperature and salinity using an open boundary condition with a sponge layer and range of restoring time scales (see Table S3). The hydrography at the boundaries is comprised of three distinct water masses: the surface water mass has a salinity of 34.15 g/kg and a temperature of -1.8 °C; below it the CDW temperature maximum has a salinity of 34.67 g/kg and a temperature of 1 °C; at the very bottom the salinity drops to 34.65 g/kg and the temperature to -0.5 °C. The properties of each water mass was selected to approximate various hydrographic profiles around Antarctica from the WOA climatology (Boyer et al., 2018). In the top 75m of the forcing profile the temperature and salinity are constant and equal to that of surface water mass to mimic a surface mixed layer. Below the mixed layer, the temperature and salinity are interpolated using a piecewise-cubic polynomial to reach the CDW temperature maximum at a depth $z = -H_{\mathrm{max}}$, which varies between simulations as discussed in the main text, and to reach the bottom water properties at the bottom of the model domain. This temperature/salinity profile is also used to restore the stratification along the eastern boundary, except the depth of the CDW temperature maximum deepens linearly toward the shelf break, simulating the presence of an Antarctic Slope Front (Thompson et al., 2018). The western boundary is an open boundary with an Orlanski radiation condition.

The flow in our simulations is also subject to the effect of unresolved sub-gridscale turbulence, which is parameterized in the following ways: First, we impose a quadratic frictional stress at the sea floor and at the based of the ice, with non-dimensional coefficient $C_d = 2.0 \times 10^{-3}$. Small-scale energy and enstrophy are controlled via a biharmonic Smagorinsky viscosity with a dimensionless coefficient of $A_{\mathrm{Smag}} = 4$ (Griffies & Hallberg, 2000), accompanied by a Laplacian vertical viscosity of $A_r = 3 \times 10^{-4}\,\mathrm{m}^2/s$. The MITgcm implementation of the KPP mixing parameterization is used. In this version of the MITgcm model (65u), the KPP parameterization creates a region of relatively large vertical diffusion ($\kappa_r \sim 0.005\mathrm{m}^2/\mathrm{s}$) that is typically one grid cell thick just under the ice shelf base. This region of large diffusion mimics the high mixing close to the ice base due to the buoyant melt plume (Lazeroms et al., 2018), which we are unable to resolve on the vertical scale of our model. This high diffusion region leads to a more realistic cavity circulation by preventing spurious numerical double diffusion at the ice face (not shown).

We use the MITgcm SHELFICE package with the simple boundary layer mixing parameterization enabled (Losch, 2008).

All cavity geometries exhibited a similar pattern of approximately steady circulation and melt that is consistent with previous studies: A warm cross-shelf bottom water current is diverted into the cavity along its eastern wall, circulates anticyclonically and exits along the westward wall (Fig. 2(d)). The southward extent and exact path of this anticyclonic current is altered by each cavity geometry's random bathymetry. This circulation pattern is qualitatively similar to previous idealized ice shelf cavity studies (e.g. Zhao et al., 2019; De Rydt et al., 2014; Rosier et al., 2023). The melt is strongest along the grounding line where warm water first makes contact with the shelf, and then along the western wall due to the resulting melt plume (see the melt rates of the reference case (Fig. S10(b)) for example). This melt pattern is also qualitatively similar to previous idealized ice shelf cavity simulations (see De Rydt et al. (2014); Rosier et al. (2023)). The cross-shelf temperature structure Fig. 2(b) shows that isosurfaces of temperature are deflected downwards along the bottom of the ice shelf face which is in agreement with previous idealized modeling studies (e.g. see Fig. 5 in De Rydt et al., 2014) and regional models see (e.g. see Fig. 2 in Nakayama et al., 2019), and conforms to the assumptions of our theory for the geostrophically-constrained transport (Section 2).

Text S3. Application of the theory to observations

Here we provide additional detail on the calculation of the parameters for our theory from the observed geometry of the near-Antarctic sea floor and the climatological hydrography over the continental slope.

To compute the terms in (6), for each point along a given ice shelf grounding line we require a corresponding hydrographic profile that is representative of conditions at the location of the HUB (*c.f.* Fig. 1). We draw these hydrographic profiles from the WOA casts just offshore of the continental shelf, approximately along the 1500m isobath that encircles Antarctica (Fig. S1), because parts of the Antarctic continental shelf have never been directly measured (See Fig. 2 of Haumann et al. (2020)). A caveat to this approach is that processes occurring across the Antarctic slope front (Thompson et al., 2018) and the continental shelf (Klinck & Dinniman, 2010; Moorman et al., 2023) may lead to hydrographic variations between the continental shelf break and the fronts of the ice shelf cavities.

We select the WOA hydrographic profile closest to the HUB for each grounding line point by combining the HUB and a breadth first search. Briefly, we first calculate the HUB, which we denote as z_{HUB}, for each grounding line point, which we denote by the vector location $\mathbf{x}_{\mathrm{GL}}$. We then seek the shortest path from $\mathbf{x} = \mathbf{x}_{\mathrm{GL}}$ to the 1500m isobath that ascends no shallower than just above z_{HUB}, *i.e.* we insist that the path follow the deepest isobath connecting $\mathbf{x}_{\mathrm{GL}}$ with the open ocean. Mathematically, this corresponds to conducting a breadth-first search that starts at $\mathbf{x} = \mathbf{x}_{\mathrm{GL}}$, that is restricted to depths satisfying $z < z_{HUB} + \epsilon$ (where ϵ is arbitrarily chosen to be 5m), and that terminates upon reaching any point $\mathbf{x} = \mathbf{x}_{1500}$ along the circum-Antarctic 1500m isobath. We then use the geographically closest WOA cast to $\mathbf{x}_{1500}$ to compute the hydrographic parameters for our theory. For example, Fig. 3(a) shows the selected WOA cast that is selected by our algorithm for a point on the grounding line of the Amery ice shelf.

Once we have found the WOA hydrographic profile for each grounding line point $\mathbf{x}_{\mathrm{GL}}$, we compute the hydrographic parameters for our theory as follows: We calculate $(\theta_{CDW} - \theta_{surf})$ as the average temperature above freezing between z_{HUB} and $z_{HUB}+100\,\mathrm{m}$, in order to mitigate observational noise (see Fig. 3(b)). In order to approximate the thickness of the CDW layer, H_{CDW}, we first estimate the depth of the pycnocline that separates surface waters from CDW. To find the depth of the pycnocline (H_{pyc}) we first smooth each density profile using a moving average with a window of 50 meters, calculate $\frac{\delta\rho}{\delta z}(z)$, and compute the average depth of all points with a $-\frac{\delta\rho}{\delta z}(z)$ above the 85th percentile. We find that this consistently captures the depth of the pycnocline while being relatively insensitive to local maxima of the density gradient elsewhere in the hydrographic profile. We then average the density 50 m above and below $z = -H_{pyc}$ to find σ_{CDW} and σ_{surf}, and thus calculate g'_{out}.

To determine a single ice shelf slope $\overline{s_{ice}}$ for each ice shelf cavity we first section the ice draft data from Bedmachine (Morlighem, 2020) using the ice shelf boundaries from MEASURES (Mouginot et al., 2017) datasets. We then compute the least squares fit of a plane $(a\mathbf{x} + b\mathbf{y} + c = z)$ to the draft of the largest continuous region of the ice shelf. We then define $s_{\mathrm{ice}} = \sqrt{a^2 + b^2}$ such that slope is the same regardless of the orientation of the plane.

We make this choice because it calculates a slope most similar to the linear slope in our idealized model configuration and is insensitive to small scale local changes in ice thickness like ridges in the ice. **Note:** we exclude at this step ice shelves with less than 100 continuous points in Bedmachine2.

The parameter α is 1.25 times larger in the modeling results when compared to the observational results. One source of this difference could be the fact that in our observational estimate we use the W_0 length scale derived from our modeling experiments, but, that length scale may be different in real ice shelves. It also may be the case that the slightly different methods we use to calculate Eq. 5 in observations compared to the models yields a factor of 1.25 difference.

Table S1.

Experiment Name	Shelf depth (m)	Random bathymetry seed	Random bathymetry amplitude (m)	Cavity depth and shelf depth difference (m)	Cavity width (m)	Ice shelf northward extent (m)
ref	650	32	0	-300	150	150
y100	650	64	250	-300	150	**100**
y250	650	64	250	-300	150	**250**
d500	**500**	16	200	-300	150	150
d600	**600**	16	200	-300	150	150
d700	**700**	16	200	-300	150	150
w50	650	32	250	-300	**50**	150
w100	650	32	250	-300	**100**	150
w250	650	32	250	-300	**250**	150
s0	900	22	250	**0**	150	150
s150	900	22	250	**150**	150	150
s300	900	22	250	**300**	150	150

Table S2.

Symbol	Definition
C_p	Specific heat of water
f	Coriolis parameter
g'_in	Reduced gravity inside of cavity
g'_out	Reduced gravity outside of cavity
H_CDW	Thickness of CDW at deepest entrance point to cavity
h_CDW	Thickness of CDW
I_f	Latent heat of melt
L	Length of Cavity (perpendicular to grounding line)
s_CDW	Slope of interface between CDW and surface waters
s_ice	Slope of ice shelf face
T	Transport of CDW into the cavity
u_CDW	velocity of CDW layer
W	Width of ice shelf cavity (parallel to grounding line)
W_0	Melt length scale
ρ_0	Reference density of water
ρ_i	Reference density of ice
θ_CDW	Potential temperature of CDW layer
θ_surf	Potential temperature of surface layer

Table S3.

Param.	Value	Description
L_x	400km	Zonal domain size
L_y	300km	Meridional domain size
H	1500m	Maximum ocean depth
L_r	20km	Sponge thickness
τ_o^{in}	10 days	Inner relaxation timescale for ocean
τ_o^{out}	12 hours	Outer relaxation timescale for ocean
f_0	$-1.3 \times 10^{-4} s^{-1}$	Reference Coriolis parameter
β	$1 \times 10^{-11} (ms)^{-1}$	Rossby parameter
C_d	2×10^{-3}	Quadratic frictional drag coefficient
A_v	$1 \times 10^{-4} m^2 s^{-1}$	Vertical eddy viscosity
Δ_x, Δ_y	2.08 km, 2.0 km	Horizontal grid spacing
Δ_z	2-200 m	Vertical grid spacing
Δ_t	75–175s	Time step

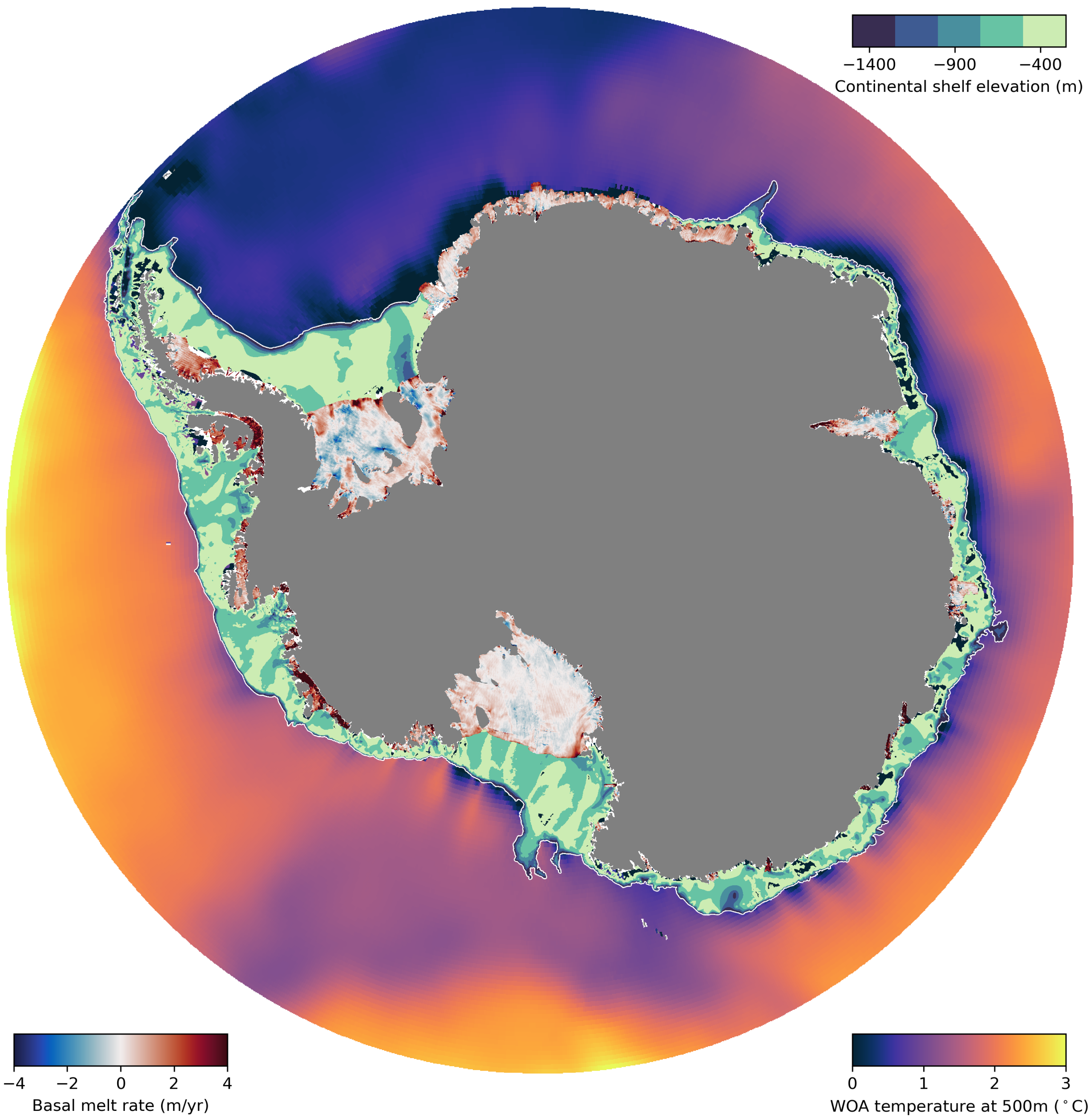

Figure S1. World Ocean Atlas (Boyer et al., 2018) temperatures at a depth of 500 m are plotted for locations with a depth greater than 1500 m. The bathymetry of the continental shelf from BedMachine2 (Morlighem, 2020) is plotted for depths shallower than 1500 m in regions that are not covered by ice shelves. Where there are ice shelves, the satellite derived basal melt rate from Adusumilli et al. (2020) is plotted.

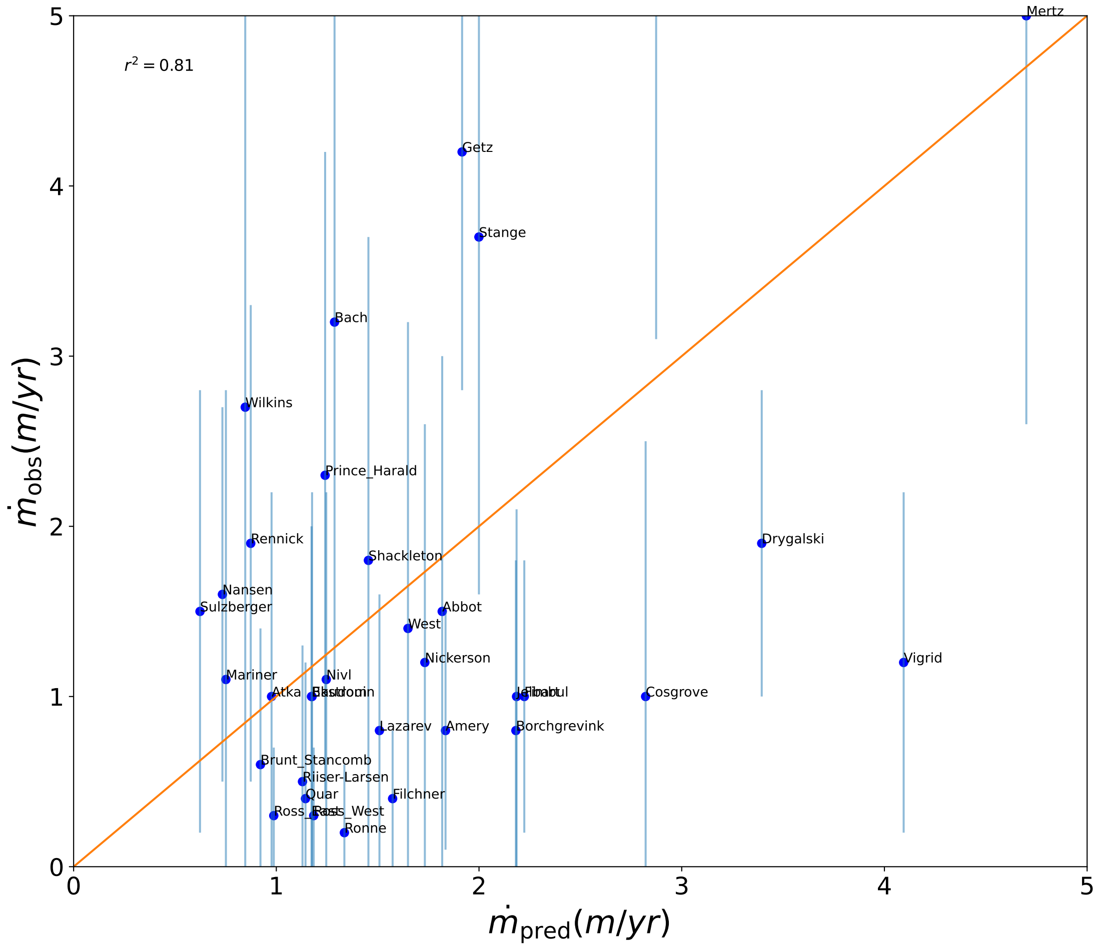

Figure S2. Same as Figure 4c, but zoomed into the bottom left corner where predicted and observed melt rates are low. Error bars are estimates of observational error from Adusumilli et al. (2020)

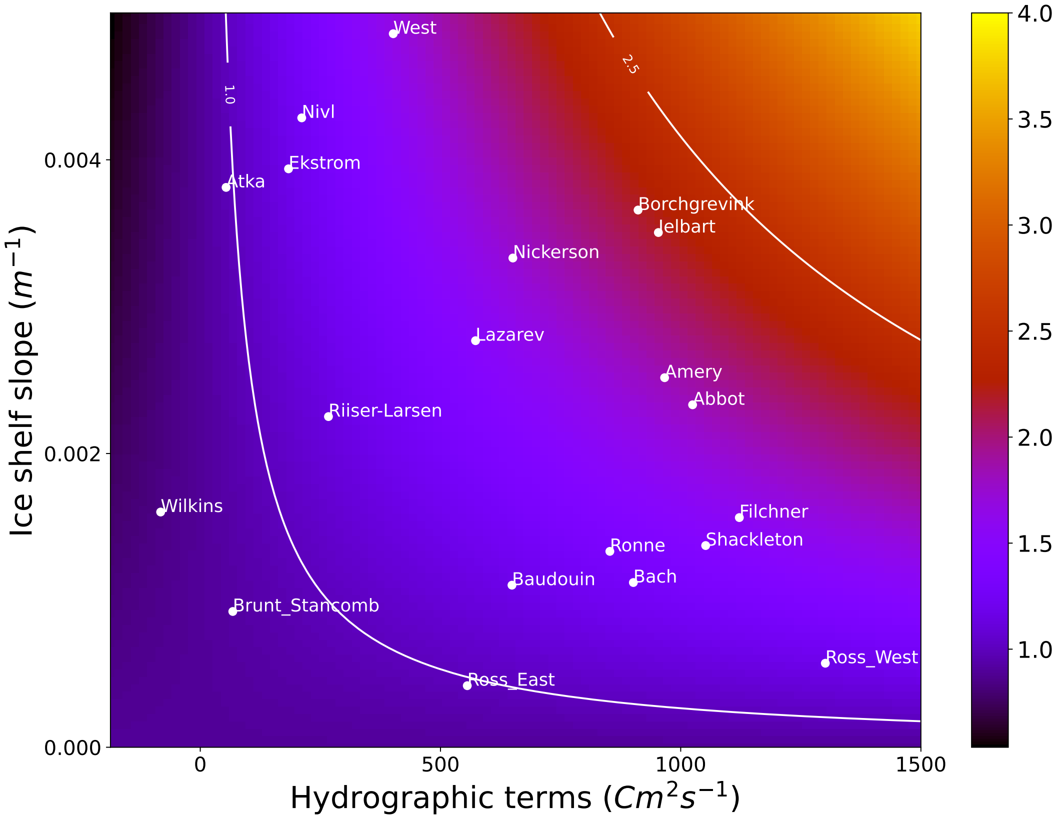

Figure S3. Same as Figure 4d, but zoomed into the bottom left corner where slope and hydrographic terms are low. The color bar magnitude has been changed from Figure 4d to better show differences in predicted melt in this smaller range.

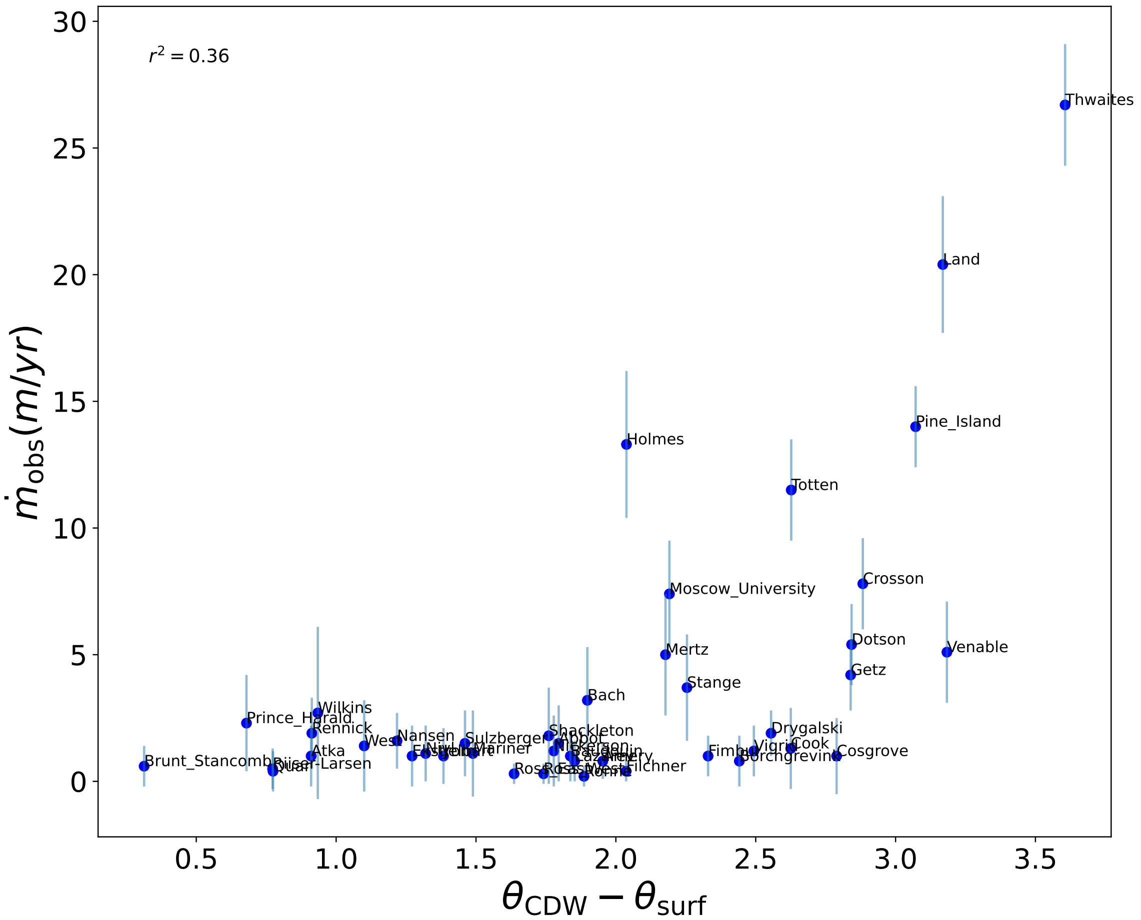

Figure S4. The thermal forcing term from Eq. 5 plotted against observed melt rates from Adusumilli et al. (2020). Error bars are estimates of observational error from Adusumilli et al. (2020).

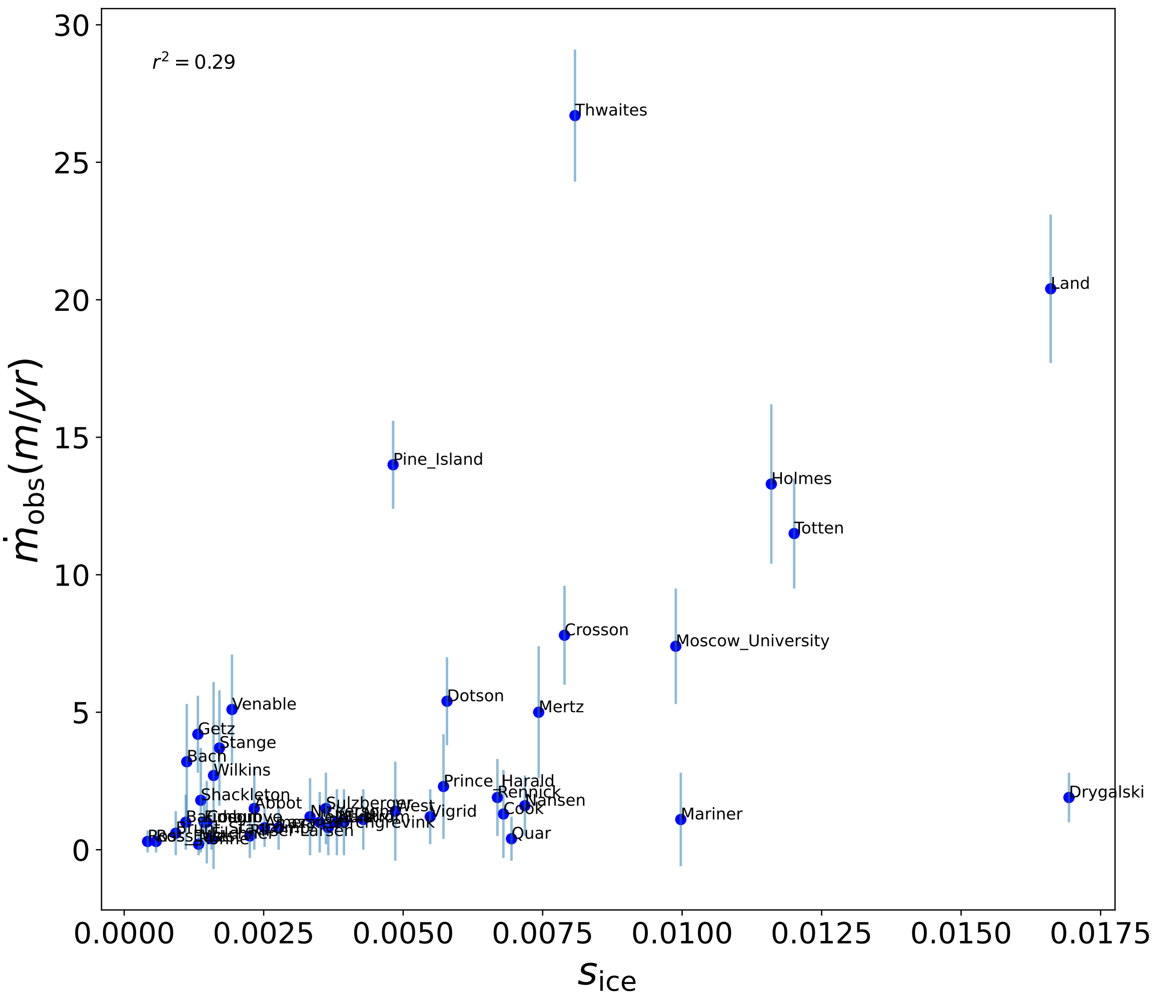

Figure S5. The slope term from Eq. 5 plotted against observed melt rates from Adusumilli et al. (2020). Error bars are estimates of observational error from Adusumilli et al. (2020).

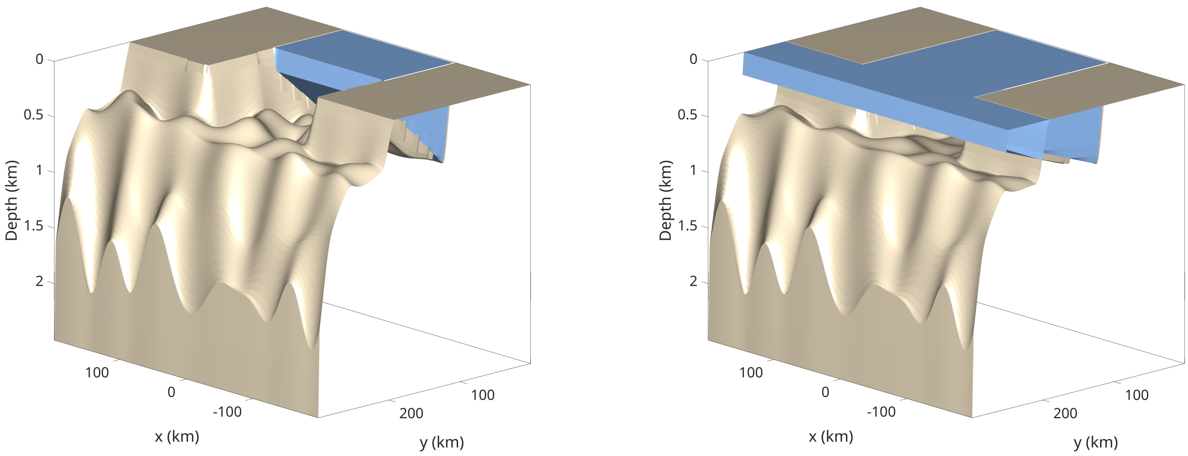

Figure S6. Model geometry of simulations with varying ice shelf extents. On the left, a simulation with an icefront of 100 km (y100). On the right, a simulation with an icefront of 250 km (y250)

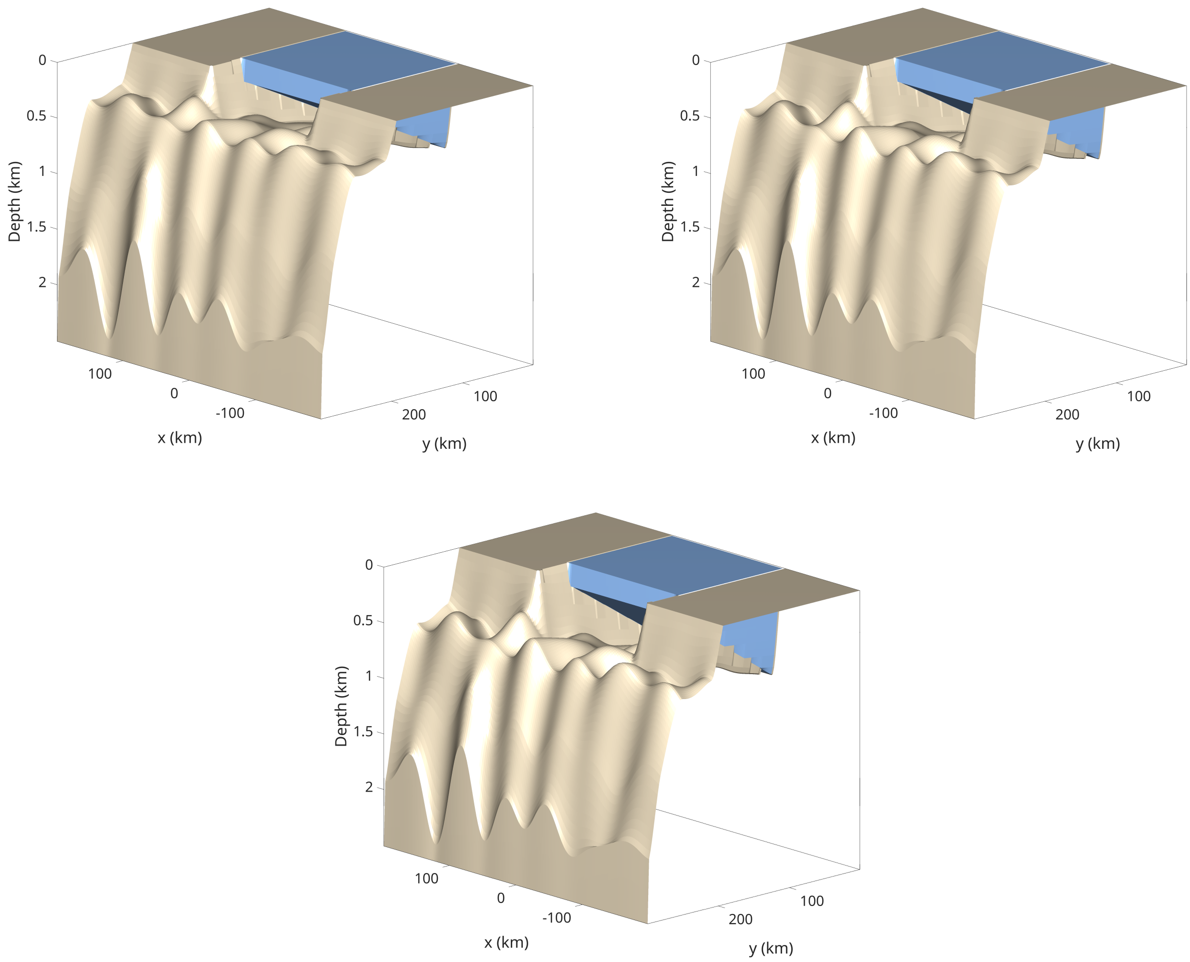

Figure S7. Model geometry of simulations with varying shelf depths. On the top left, a simulation with a depth of 500 m (d500). On the top right, a simulation with a shelf depth of 600 m (d600). On the bottom, a simulation with a shelf depth of 700 m (d700).

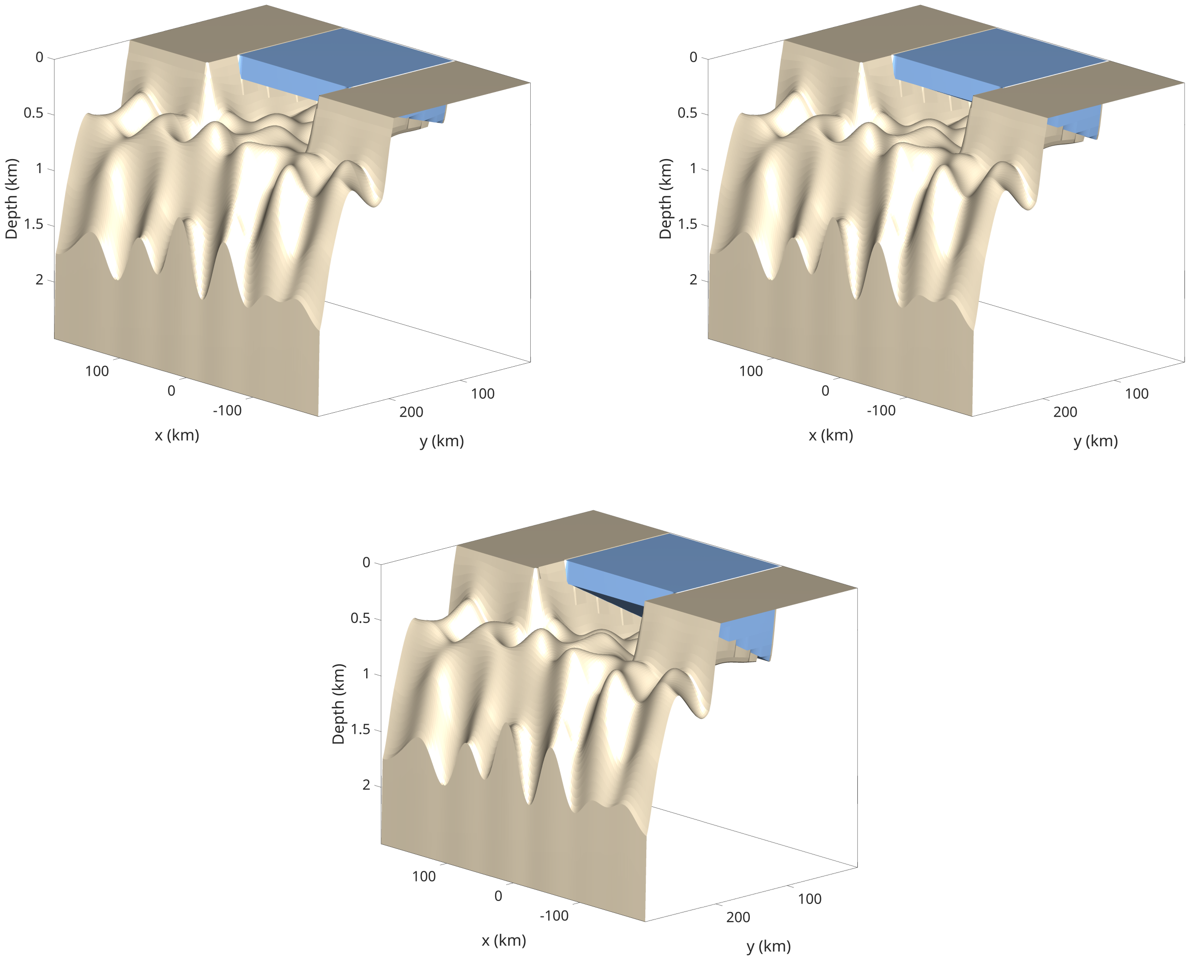

Figure S8. Model geometry of simulations with varying bed slopes. On the top left, a simulation with a continental shelf 300 m deeper than the grounding line (s300). On the top right, a simulation with a continental shelf 150 m deeper than the grounding line (s150). On the bottom, a simulation with a continental shelf 0 m deeper than the grounding line (s0).

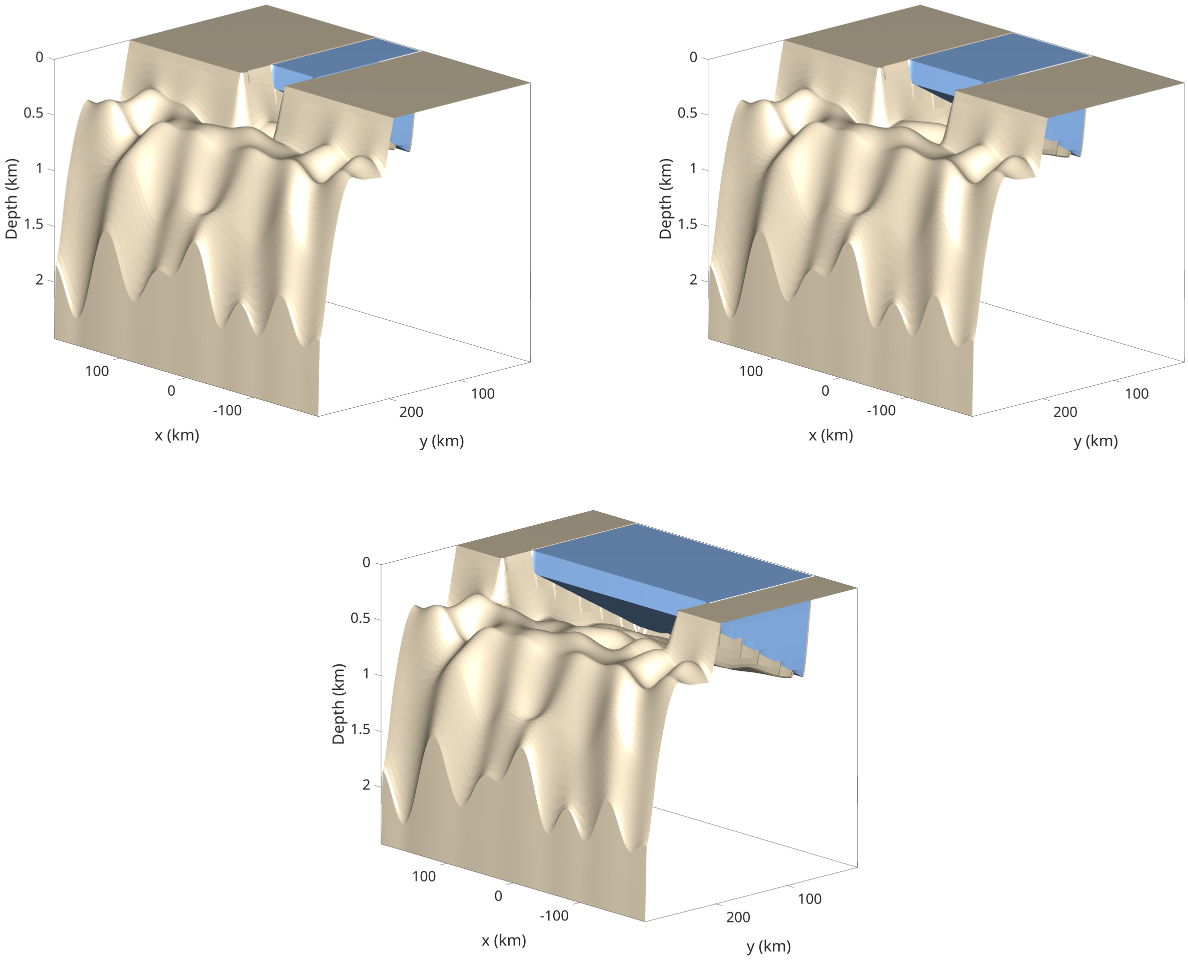

Figure S9. Model geometry of simulations with varying cavity widths. On the top left, a simulation with a continental shelf 50 km wide (w50). On the top right, a simulation with a continental shelf 100 km wide (w100). On the bottom, a simulation with a continental shelf 250 km wide (w250).

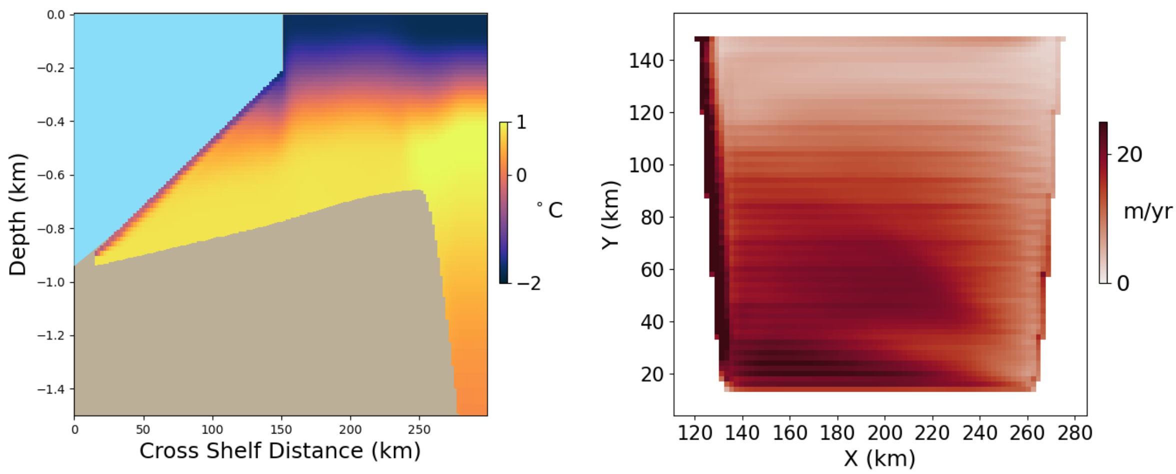

Figure S10. Meridional cross sections of time-average potential temperature (left column) and maps of time-average ice shelf melt in m/yr (right column) from high thermocline model simulations with reference geometry.

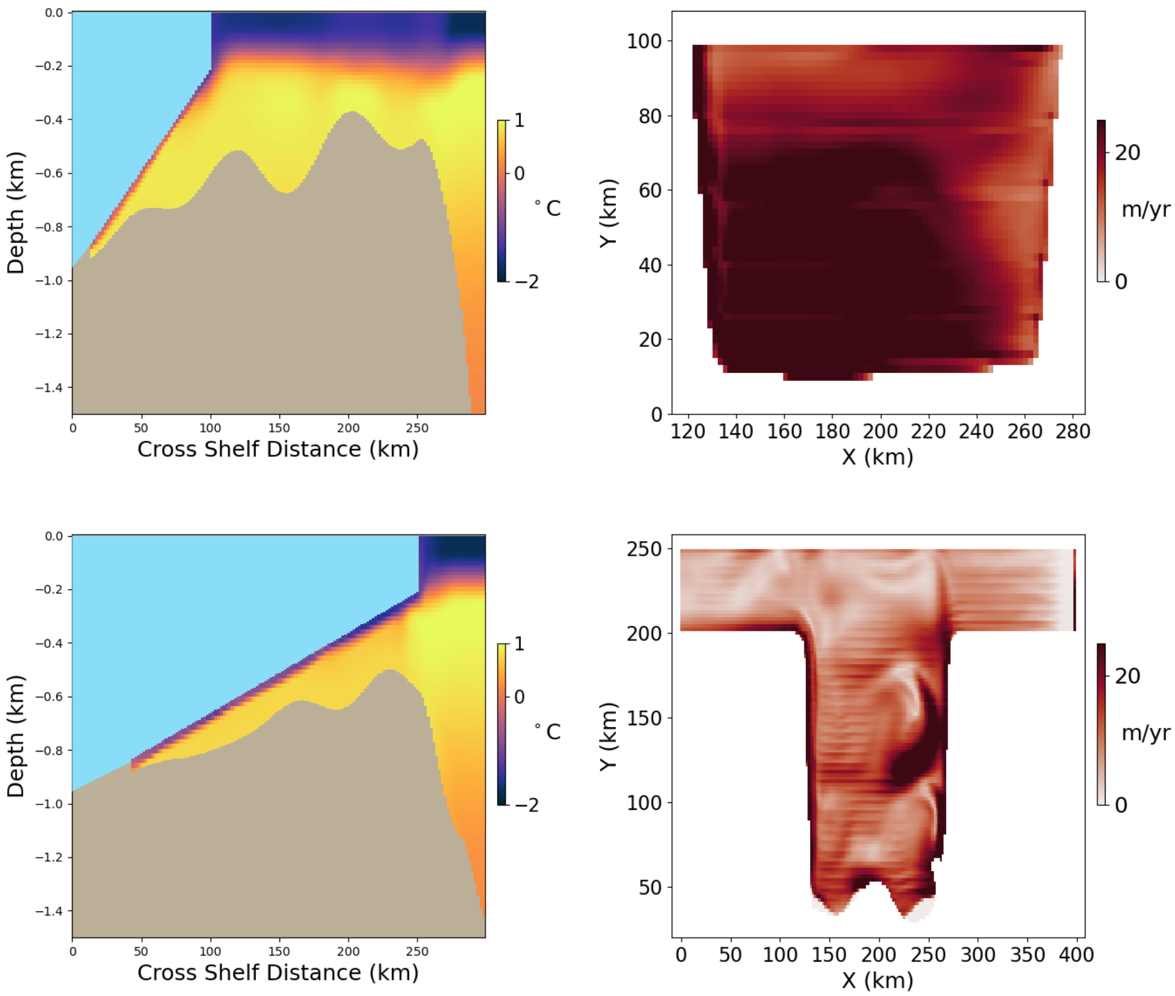

Figure S11. Meridional cross sections of time-average potential temperature (left column) and maps of time-average ice shelf melt in m/yr (right column) from high thermocline model simulations with varying ice shelf extent. At the top a simulation with an icefront of 100 km (y100). On the bottom, a simulation with an icefront of 250 km (y250)

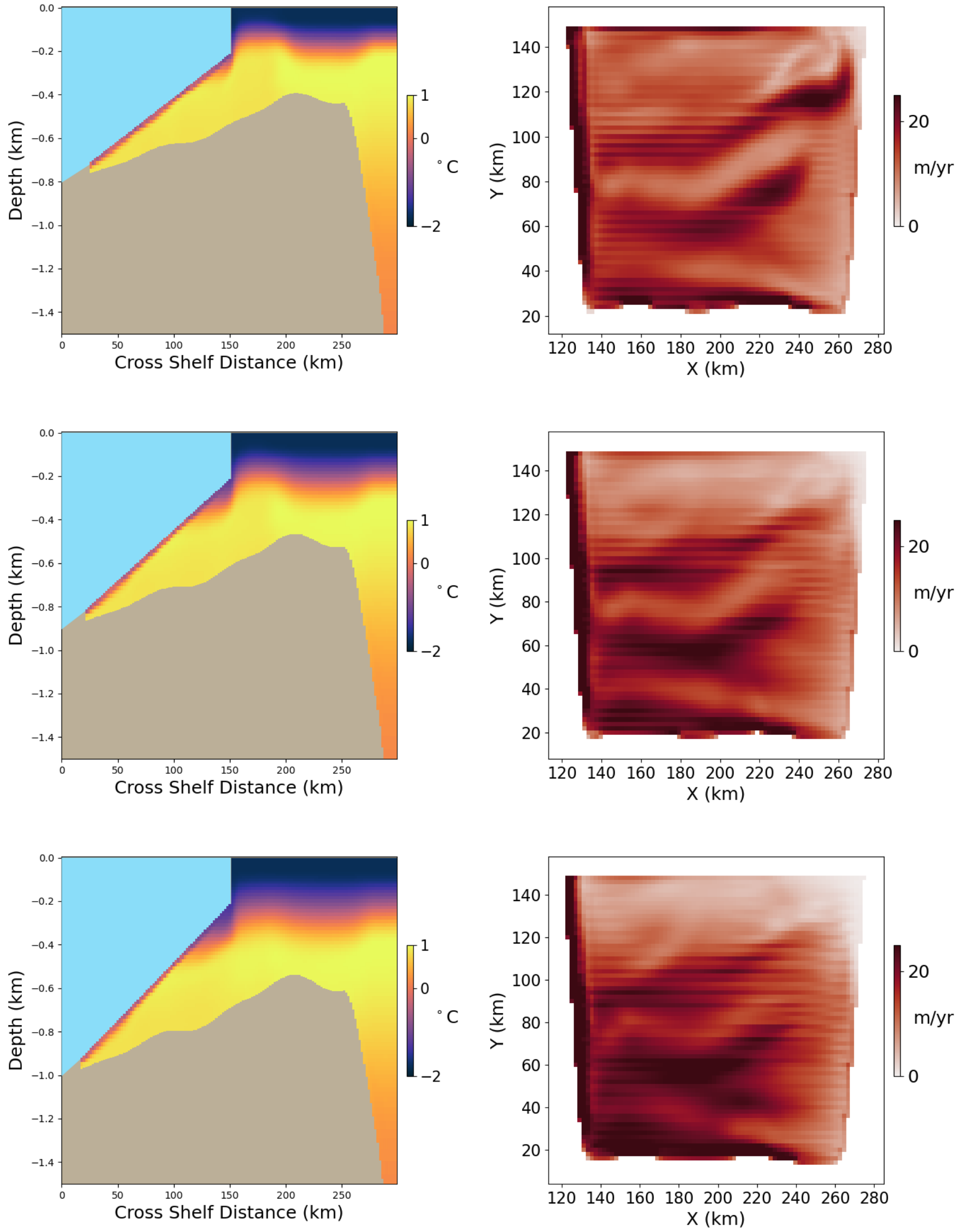

Figure S12. Meridional cross sections of time-average potential temperature (left column) and maps of time-average ice shelf melt in m/yr (right column) from high thermocline model simulations with varying shelf depths. At the top , a simulation with a depth of 500 m (d500). In the middle, a simulation with a shelf depth of 600 m (d600). On the bottom, a simulation with a shelf depth of 700 m (d700).

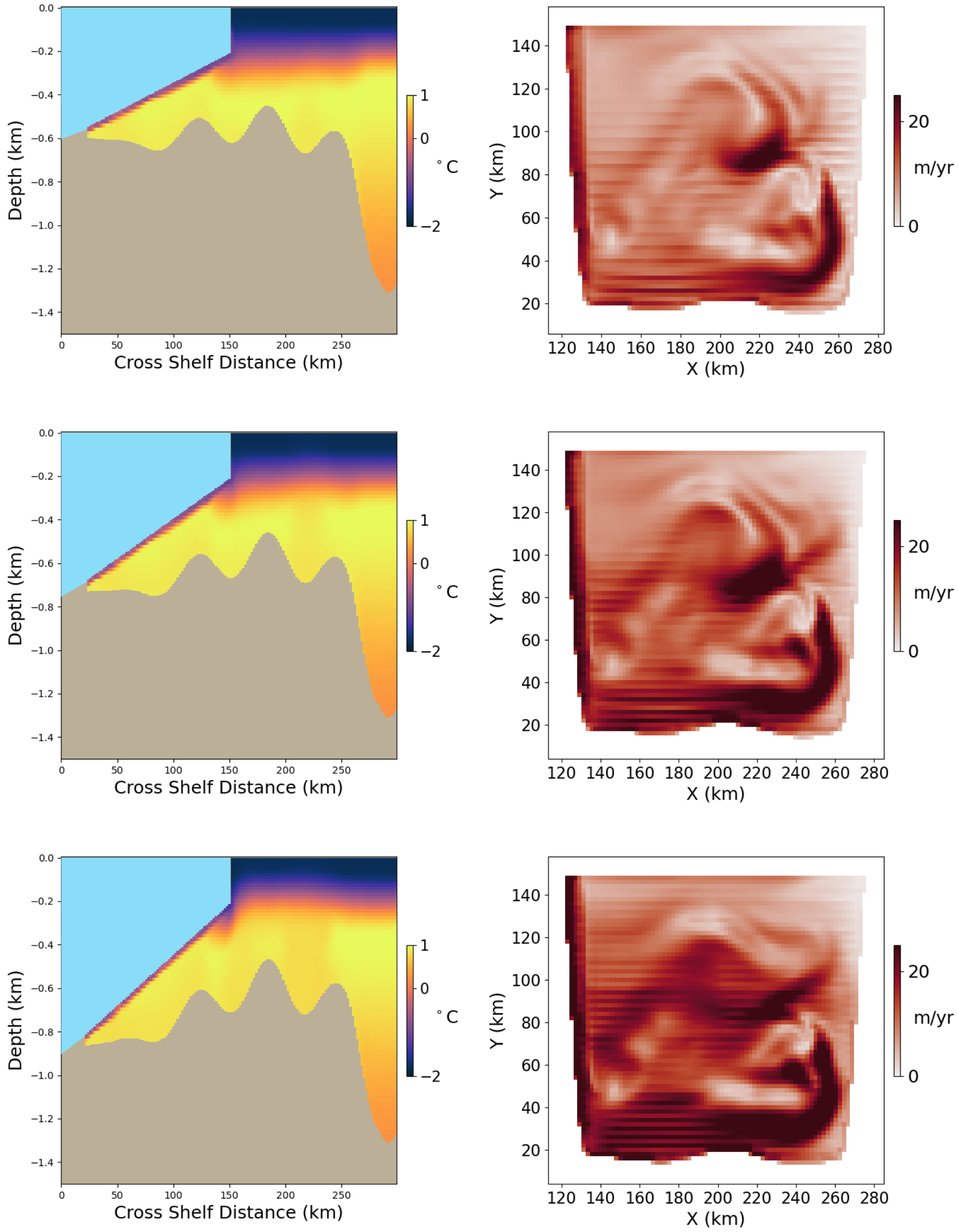

Figure S13. Meridional cross sections of time-average potential temperature (left column) and maps of time-average ice shelf melt in m/yr (right column) from high thermocline model simulations with varying bed slopes. On the top, a simulation with a continental shelf 300 m deeper than the grounding line (s300). In the middle, a simulation with a continental shelf 150 m deeper than the grounding line (s150). On the bottom, a simulation with a continental shelf 0 m deeper than the grounding line (s0).

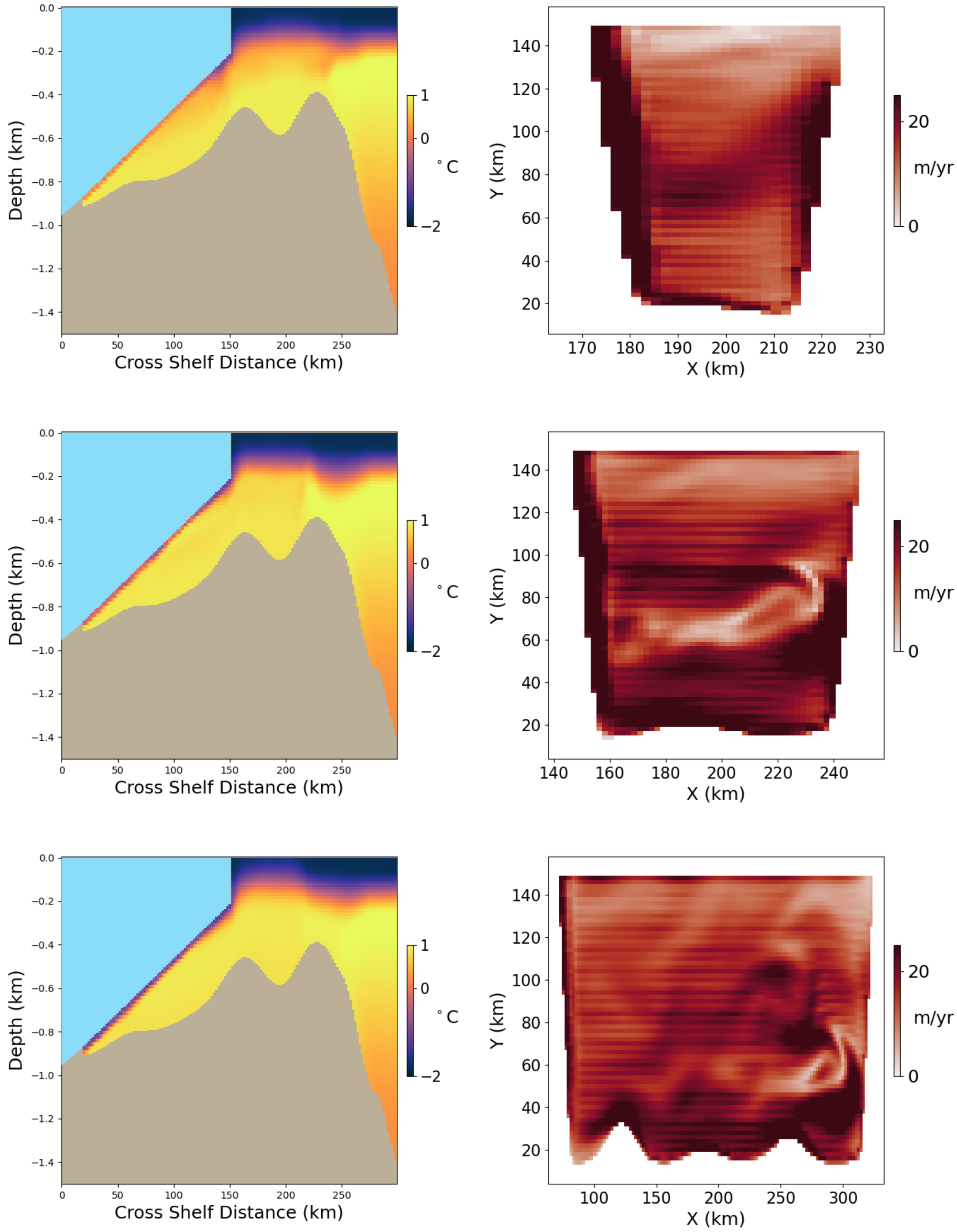

Figure S14. Meridional cross sections of time-average potential temperature (left column) and maps of time-average ice shelf melt in m/yr (right column) from high thermocline model simulations with varying cavity widths. On the top, a simulation with a continental shelf 50 km wide (w50). In the middle, a simulation with a continental shelf 100 km wide (w100). On the bottom, a simulation with a continental shelf 250 km wide (w250).

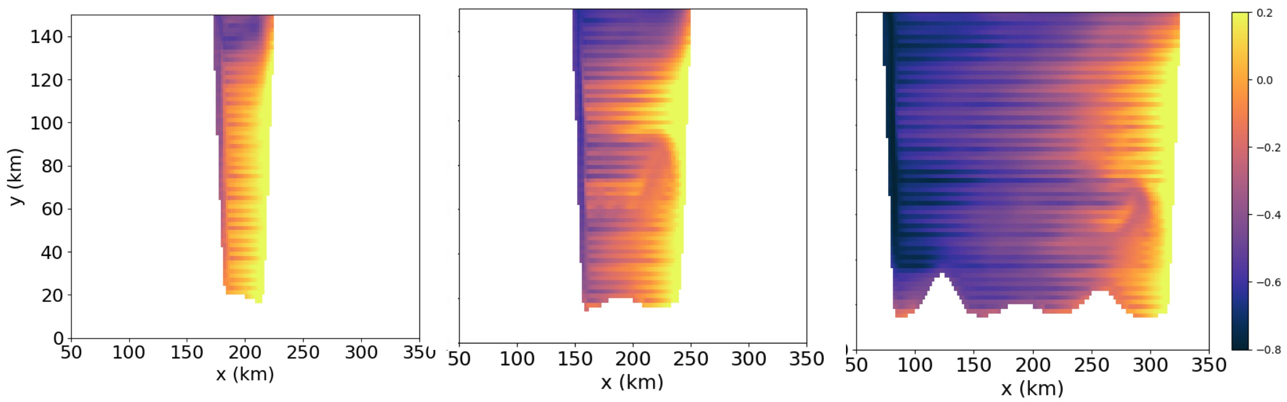

Figure S15. Maps of time average potential temperature directly below ice shelf face in high thermocline simulations with varying widths. On the left, a simulation with a continental shelf 50 km wide (w50). In the middle, a simulation with a continental shelf 100 km wide (w100). On the right, a simulation with a continental shelf 250 km wide (w250).

References

Adusumilli, S., Fricker, H. A., Medley, B., Padman, L., & Siegfried, M. R. (2020). Interannual variations in meltwater input to the Southern Ocean from Antarctic ice shelves. *Nature Geoscience*, *13*(9), 616–620. doi: 10.1038/s41561-020-0616-z

Boyer, T. P., Garcia, H. E., Locarnini, R. A., Zweng, M. M., Mishonov, A. V., Reagan, J. R., ... Smolyar, I. V. (2018). *World ocean atlas 2018.* NOAA National Centers for Environmental Information.

De Rydt, J., Holland, P. R., Dutrieux, P., & Jenkins, A. (2014). Geometric and oceanographic controls on melting beneath Pine Island Glacier. *Journal of Geophysical Research: Oceans*, *119*(4), 2420–2438. doi: 10.1002/2013JC009513

Griffies, S. M., & Hallberg, R. W. (2000). Biharmonic friction with a Smagorinsky-like viscosity for use in large-scale eddy-permitting ocean models. *Mon. Weather Rev.*, *128*(8), 2935–2946.

Haumann, F. A., Moorman, R., Riser, S. C., Smedsrud, L. H., Maksym, T., Wong, A. P. S., ... Sarmiento, J. L. (2020). Supercooled Southern Ocean Waters. *Geophysical Research Letters*, *47*(20), e2020GL090242. doi: 10.1029/2020GL090242

Klinck, J. M., & Dinniman, M. S. (2010). Exchange across the shelf break at high southern latitudes. *Ocean Science*, *6*(2), 513–524. doi: 10.5194/os-6-513-2010

Lazeroms, W. M. J., Jenkins, A., Gudmundsson, G. H., & van de Wal, R. S. W. (2018). Modelling present-day basal melt rates for Antarctic ice shelves using a parametrization of buoyant meltwater plumes. *The Cryosphere*, *12*(1), 49–70. doi: 10.5194/tc-12-49-2018

Losch, M. (2008). Modeling ice shelf cavities in a z coordinate ocean general circulation model.

Journal of Geophysical Research: Oceans, *113*(C8). doi: 10.1029/2007JC004368

McDougall, T. J., Jackett, D. R., Wright, D. G., & Feistel, R. (2003). Accurate and Computationally Efficient Algorithms for Potential Temperature and Density of Seawater. *Journal of Atmospheric and Oceanic Technology*, *20*(5), 730–741. doi: 10.1175/1520-0426(2003)20⟨730:AACEAF⟩2.0.CO;2

Moorman, R., Thompson, A. F., & Wilson, E. A. (2023). Coastal Polynyas Enable Transitions Between High and Low West Antarctic Ice Shelf Melt Rates. *Geophysical Research Letters*, *50*(16), e2023GL104724. doi: 10.1029/2023GL104724

Morlighem, M. (2020). *Measures bedmachine antarctica, version 2.* NASA National Snow and Ice Data Center Distributed Active Archive Center.

Mouginot, J., Scheuchl, B., & Rignot, E. (2017). *Measures antarctic boundaries for ipy 2007-2009 from satellite radar, version 2.* NASA National Snow and Ice Data Center Distributed Active Archive Center.

Nakayama, Y., Manucharyan, G., Zhang, H., Dutrieux, P., Torres, H. S., Klein, P., … Menemenlis, D. (2019). Pathways of ocean heat towards Pine Island and Thwaites grounding lines. *Scientific Reports*, *9*(1), 16649. doi: 10.1038/s41598-019-53190-6

Rosier, S. H. R., Bull, C. Y. S., Woo, W. L., & Gudmundsson, G. H. (2023). Predicting ocean-induced ice-shelf melt rates using deep learning. *The Cryosphere*, *17*(2), 499–518. doi: 10.5194/tc-17-499-2023

Thompson, A. F., Stewart, A. L., Spence, P., & Heywood, K. J. (2018). The Antarctic Slope Current in a Changing Climate. *Reviews of Geophysics*, *56*(4), 741–770. doi: https://doi.org/10.1029/2018RG000624

Zhao, K. X., Stewart, A. L., & McWilliams, J. C. (2019). Sill-Influenced Exchange Flows in Ice Shelf Cavities. *Journal of Physical Oceanography*, *49*(1), 163–191. doi: 10.1175/JPO-D-18-0076.1